Paleoceanography and Paleoclimatology

AGU ADVANCING EARTH AND SPACE SCIENCE

RESEARCH ARTICLE
10.1029/2022PA004565

The Late Miocene-Early Pliocene Biogenic Bloom: An Integrated Study in the Tasman Sea

M. E. Gastaldello[1,2], C. Agnini[1], T. Westerhold[3], A. J. Drury[4], R. Sutherland[5], M. K. Drake[6], A. R. Lam[7], G. R. Dickens[8], E. Dallanave[9], S. Burns[10], and L. Alegret[2,11]

[1]Dipartimento di Geoscienze, Università degli Studi di Padova, Padova, Italy, [2]Departamento de Ciencias de la Tierra, Universidad de Zaragoza, Zaragoza, Spain, [3]MARUM-Center for Marine Environmental Sciences, University of Bremen, Bremen, Germany, [4]Department of Earth Sciences, University College London, London, UK, [5]Victoria University of Wellington, Wellington, New Zealand, [6]Ocean Sciences Department, University of California, Berkeley, CA, USA, [7]Department of Geological Sciences and Environmental Studies, Binghamton University, Binghamton, NY, USA, [8]Trinity College Dublin, Dublin, Ireland, [9]Faculty of Geosciences, University of Bremen, Bremen, Germany, [10]Department of Geosciences, University of Massachusetts Amherst, Amherst, MA, USA, [11]Instituto de Investigación en Ciencias Ambientales de Aragón, Universidad de Zaragoza, Zaragoza, Spain

Key Points:

- We construct an integrated age model (7.4–4.5 Ma) for Site U1506 beneath the subtropical return flow of the South Pacific Gyre
- Benthic foraminifera reveal high productivity and a local change in oceanography during the Late Miocene to Early Pliocene Biogenic Bloom
- Stronger intermediate depth bottom currents before 6.7 Ma suggest a weakening of shallow wind driven Pacific Ocean circulation at 6.7 Ma

Supporting Information:

Supporting Information may be found in the online version of this article.

Correspondence to:

M. E. Gastaldello,
mariaelena.gastaldello@phd.unipd.it

Citation:

Gastaldello, M. E., Agnini, C., Westerhold, T., Drury, A. J., Sutherland, R., Drake, M. K., et al. (2023). The late miocene-early pliocene biogenic bloom: An integrated study in the Tasman Sea. *Paleoceanography and Paleoclimatology*, *38*, e2022PA004565. https://doi.org/10.1029/2022PA004565

Received 7 OCT 2022
Accepted 20 FEB 2023

Author Contributions:

Conceptualization: M. E. Gastaldello, C. Agnini, A. J. Drury, R. Sutherland, G. R. Dickens, L. Alegret
Data curation: M. E. Gastaldello
Investigation: M. E. Gastaldello, T. Westerhold, M. K. Drake, A. R. Lam, S. Burns
Supervision: C. Agnini, L. Alegret
Writing – original draft: M. E. Gastaldello

Abstract The Late Miocene-Early Pliocene Biogenic Bloom (~9–3.5 Ma) was a paleoceanographic phenomenon defined by anomalously high accumulations of biological components at multiple open ocean sites, especially in certain regions of the Indian, and Pacific oceans. Its temporal and spatial extent with available information leaves fundamental questions about driving forces and responses unanswered. In this work, we focus on the middle part of the Biogenic Bloom (7.4–4.5 Ma) at International Ocean Discovery Program Site U1506 in the Tasman Sea, where we provide an integrated age model based on orbital tuning of the Natural Gamma Radiation, benthic foraminiferal oxygen isotopes, and calcareous nannofossil biostratigraphy. Benthic foraminiferal assemblages suggest changes in deep water oxygen concentration and seafloor nutrient supply during generally high export productivity conditions. From 7.4 to 6.7 Ma, seafloor conditions were characterized by episodic nutrient supply, perhaps related to seasonal phytoplankton blooms. From 6.7 to 4.5 Ma, the regime shifted to a more stable interval characterized by eutrophic and dysoxic conditions. Combined with seismic data, a regional change in paleoceanography is inferred at around 6.7 Ma, from stronger and well-oxygenated bottom currents to weaker, oxygen-depleted bottom currents. Our results support the hypothesis that the Biogenic Bloom was a complex, multiphase phenomenon driven by changes in ocean currents, rather than a single uniform period of sustained sea surface water productivity. Highly resolved studies are thus fundamental to its understanding and the disentanglement of local, regional, and global imprints.

1. Introduction

The Late Miocene-Early Pliocene was an interval of major changes in global tectonics, climate, and oceanography (Haywood et al., 2009; Steinthorsdottir et al., 2021). Significant events include the closing of the Isthmus of Panama, primary and renewed uplift of the Andes and Himalayas respectively, isolation of the Mediterranean, expansion of Antarctic ice, spreading of C_4 vegetation, intensification of monsoonal activity, and a general cooling of surface and deep ocean water masses (Cerling et al., 1997; Herbert et al., 2016; Holbourn et al., 2018; Molnar et al., 1993; Prell & Kutzbach, 1992; Quade & Cerling, 1995; Steinthorsdottir et al., 2021; Westerhold et al., 2020; Zachos et al., 2001; Zhisheng et al., 2001).

A notable paleoceanographic phenomenon also occurred across this time interval, generally referred to as the "Late Miocene to Early Pliocene Biogenic Bloom" (Farrell et al., 1995). At numerous locations, especially beneath upwelling regions of the Pacific (Berger et al., 1993; Farrell et al., 1995; Lyle et al., 2019) and Indian Oceans (Peterson et al., 1992), mass accumulation rates of $CaCO_3$ and other biogenic components (e.g., Si, P, Ba) to the seafloor increased significantly between 9.0 and 3.5 Ma (Dickens & Owen, 1999; Diester-Haass et al., 2005; Farrell et al., 1995). Furthermore, at multiple locations, diatom assemblages associated with high productivity thrived, while benthic foraminiferal assemblages dominated by suboxic and dysoxic taxa (e.g., uvigerinids and buliminids) and sediment geochemistry (e.g., decreased Mn/Sc) point to low dissolved oxygen concentration at intermediate water depths (Dickens & Owen, 1994; Farrell et al., 1995; Gupta & Thomas, 1999; Lyle et al., 2019; Nomura, 1995).

Writing – review & editing: M. E. Gastaldello, C. Agnini, T. Westerhold, A. J. Drury, R. Sutherland, M. K. Drake, A. R. Lam, G. R. Dickens, E. Dallanave, L. Alegret

The Biogenic Bloom presents a paleoceanographic puzzle: marine sedimentary records strongly suggest a major increase in primary productivity across several widely separated low-latitude oceanic regions; however, such production is limited by the availability of nutrients, whose residence times are fairly short in the global ocean ($<10^5$ years; Delaney & Filippelli, 1994; Toggweiler, 1999). How therefore can widespread elevated ocean productivity be maintained for several millions of years? Two basic end-member explanations emerge although both may have transpired: (a) a greater supply of nutrients entered the ocean, or (b) nutrients within the ocean were more heterogeneous relative to present-day (and to the Late Pliocene). Within the framework of the first explanation, uplift of the Himalayas and intensification of monsoon-related weathering might have enhanced nutrient delivery to the oceans (Berger & Stax, 1994; Berger et al., 1993; Delaney & Filippelli, 1994; Farrell et al., 1995; Filippelli, 1997; Hermoyian & Owen, 2001). The second explanation refers to an extensive reorganisation of ocean circulation, which might have focused nutrients toward the photic zone in certain areas, even more than at present-day. For example, deep-water formation in the North Pacific and active Pacific meridional overturning circulation (PMOC), which no longer exist, occurred in the past (Burls et al., 2017; Shankle et al., 2021). Previous works highlight regional diversity in the duration and expression of the Biogenic Bloom (Dickens & Owen, 1999; Liao & Lyle, 2014; Lyle et al., 2019; Sutherland et al., 2019), and high-resolution studies at diverse locations are needed to more fully understand the phenomenon.

In this study, we investigate the expression of the Biogenic Bloom at International Ocean Discovery Program (IODP) Expedition 371 Site U1506 located in the central Tasman Sea (Sutherland et al., 2019). The area is a target for late Neogene paleoceanographic studies (e.g., Grant & Dickens, 2002; Kennett & Von der Borch, 1986; Sutherland et al., 2022) due to its relatively shallow water depth above the CCD and its position under the return flow of the South Pacific Gyre. Recent work at Site U1506 shows that linear sedimentation rates (LSRs) peaked between 8 and 3 Ma (Sutherland et al., 2019, 2022).

Here, we build an age model based on a high-resolution bio-astrochronological framework that enables precise dating of sediment deposited between 7.4 and 4.2 Ma at Site U1506. A crucial source of information is deep-sea sediments, which preserve benthic foraminifera that are proxies of ancient nutrient availability and oxygen conditions at the seafloor (Murray, 2006) and, hence reveal the evolution of productivity during the Biogenic Bloom. We carried out quantitative analyses of benthic foraminiferal assemblages, combined with other independent proxies, to understand the regional and global imprint of the Biogenic Bloom.

2. Materials and Methods

2.1. Location and Study Material

Site U1506 (28.66°S, 161.74°E; 1,505 m water depth) comprises a single hole (Hole 1506A) located on the northern part of Lord Howe Rise (LHR), a broad bathymetric high and submerged part of the northern Zealandia (Mortimer et al., 2017) (Figure 1). The primary rationale for drilling Site U1506 was to determine the composition of a buried ∼100 m high structure identified on seismic reflection lines (Figure 2). Drilling showed this basement structure to be composed of basalt (Sutherland et al., 2018, 2019), but also retrieved much of the overlying 265 m sediment column.

The sedimentary sequence recovered at Site U1506 was divided into units and subunits based on lithology. Samples analyzed in this work come from Subunit Ia, the uppermost 258 m of "homogenous white nannofossil ooze/chalk with foraminifera" (Sutherland et al., 2019). Because of time and goals, this sequence was recovered by rotary core barrel (RCB) drilling methods. This drilling method resulted in incomplete recovery of Site U1506 cores (typically 60%–80%) and somewhat limits the precise comparison of sedimentation rates and mass accumulation data with those at other locations.

The depth scale adopted in this work is meters CSF-A (https://www.iodp.org/policies-and-guidelines), which assumes all cores (even if incomplete) tie to the top of each drilled interval (Sutherland et al., 2019). The top 48 m (Cores 1R through 6R) are variably soupy and disturbed by drilling, whereas the underlying 195 m (Cores 8R through 26R) are moderately biscuited and fractured. We focus on a ∼140 m thick interval from Core 10R to Core 25R (81.75–233.50 m), which spans from the Late Miocene to the Early Pliocene. Sediments consist of white to greyish-white ooze and chalk with a carbonate content ranging between 88% and 95%, containing some black opaque minerals identified as pyrite. Deposition was in a lower bathyal environment, similar to that of present-day (Sutherland et al., 2019, 2022).

10.1029/2022PA004565

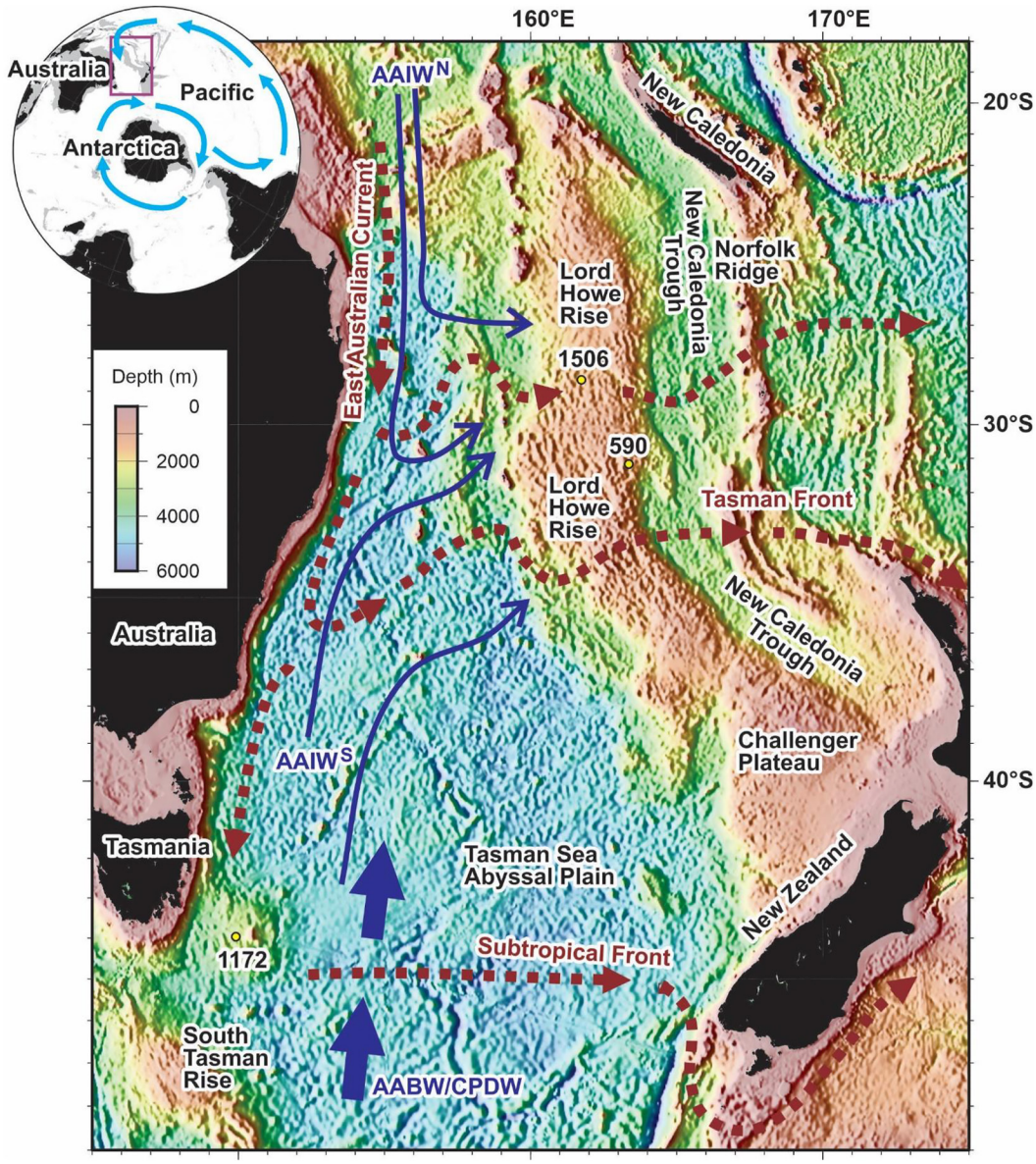

Figure 1. Circulation patterns in the Tasman Sea at present-day. Red arrows show the surface water circulation, including East Australian Current, Tasman Front and Subtropical Front; thin blue arrows indicate the intermediate waters flowing into the Tasman Sea from the north ($AAIW^N$) and the south ($AAIW^S$); thick blue arrows show deep waters (Circumpolar Deep Water and Antarctic Bottom Water), which enter the Tasman Sea from the south. Upper left: light blue arrows show the surface circulation in the South Pacific Ocean and in the Southern Ocean (the South Pacific Gyre and the Antarctic Circumpolar Current, respectively).

2.2. Oceanographic Setting

Present-day surface circulation above Site U1506 is highly influenced by the East Australian Current (EAC), a subtropical western boundary current in the southwest Pacific that flows south along the eastern edge of Australia and branches eastward towards northern New Zealand at 30°–35°S latitude (Baird et al., 2008; Hassler et al., 2011). This "eastern extension of the EAC" (Oke et al., 2019) which flows between Australia and northern New Zealand, is referred to as the Tasman Front. The Tasman Front is a divergence zone, characterized by the presence of many anticyclonic eddies and by upwelling (Marchesiello & Middleton, 2000; Stanton, 1981).

At intermediate depths between 700 and 1,500 m, two water masses enter the Tasman Sea (Figure 1). The main one is the Antarctic Intermediate Water (AAIW), entering from the northeast through the Coral Sea. This water mass is a component of the South Pacific subtropical gyre and is distinguished by low temperatures, low salinity, high

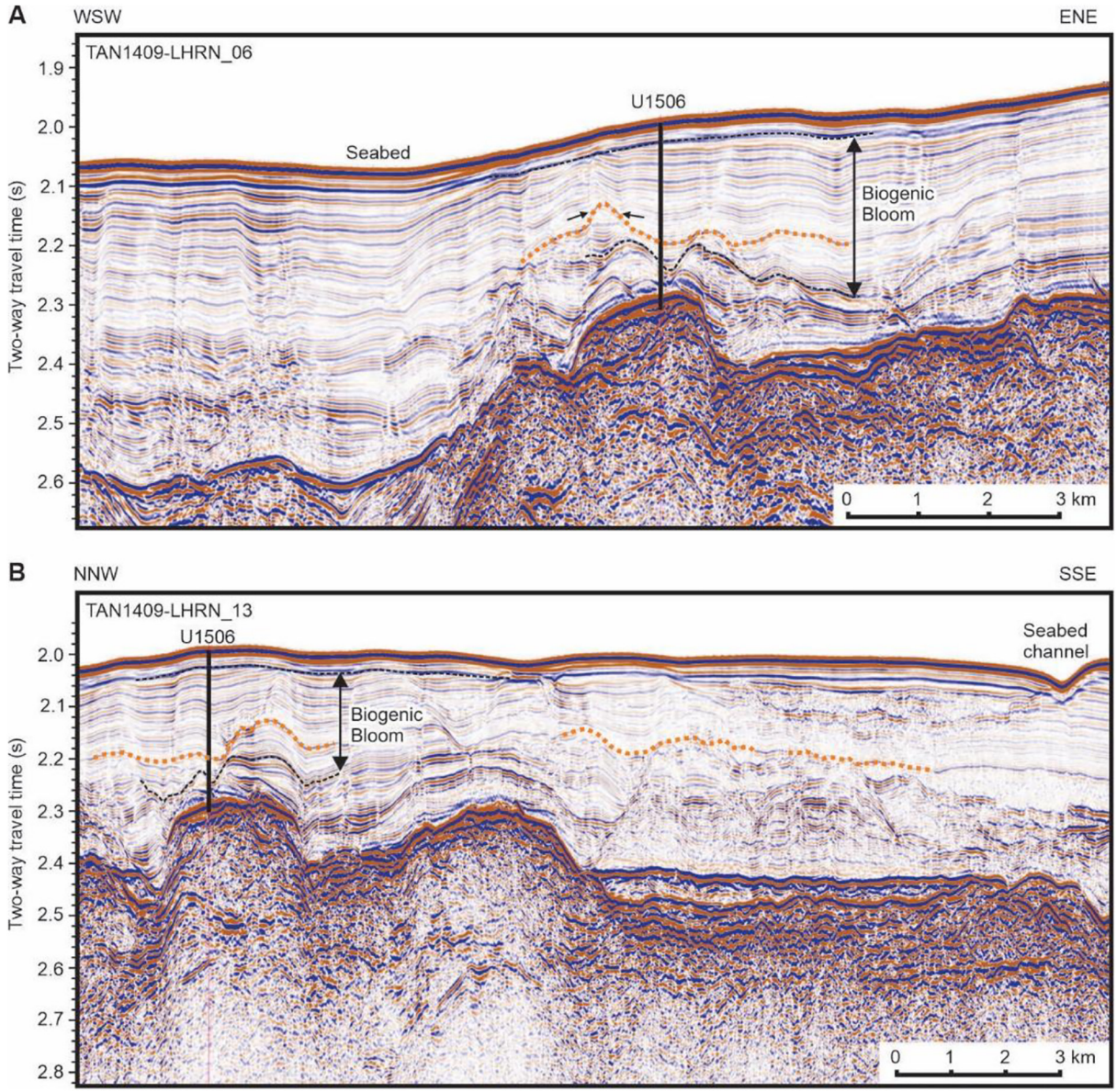

Figure 2. Seismic reflection images of local stratigraphy in the vicinity of Site U1506 (after Sutherland et al., 2022), which is located near the top of Lord Howe Rise in ~1,500 m water depth. The relatively thick Biogenic Bloom sequence has clear reflectors at its top and base (dashed black lines). A positive polarity reflector (orange dotted line) with onlapping surface above is identified with age 6.7 Ma and correlates with significant changes in faunal composition in cores (see main text).

dissolved oxygen levels, and high $\delta^{13}C$ of dissolved inorganic carbon. The second most important influence comes from intermediate waters entering from the south Tasman Sea and is characterized by higher salinity. Bostock et al. (2004) distinguished the two intermediate water masses, naming them respectively $AAIW^N$ and $AAIW^S$.

Below the AAIW, two deep-water masses enter the Tasman Sea from the south, the shallower Circumpolar Deep Water (CPDW) and the deeper Antarctic Bottom Water (AABW). The AABW has lower temperatures and higher dissolved oxygen concentrations than the CPDW (Bostock et al., 2004; Tomczak & Godfrey, 1994).

2.3. Micropaleontological Studies

Calcareous nannofossil samples were prepared using the standard "smear slide" method (Bown & Young, 1998), and biostratigraphic results are based on semi-quantitative analyses of 56 samples between 233.50 and 81.75 m (Table S1), with an average sampling resolution of 2.8 m, which equals to 86 kyr reso-

lution (Text S1 in Supporting Information S1). The biostratigraphic schemes adopted are the traditional biozonations of Martini (1971), Okada and Bukry (1980), and the one more recently proposed by Backman et al. (2012).

Quantitative studies on benthic foraminifera were carried out on 55 samples between 221.75 and 82.01 m (Text S2 in Supporting Information S1), with an average sampling resolution of 2.2 m, which represents ca. 40 kyr resolution. Bulk sediment samples were dried in an oven at 40°C and weighed to obtain bulk dry sample mass. Then they were disaggregated in water with diluted $(NaPO_3)_6$ and washed through a sieve to isolate the greater than 63 μm size fraction. Resulting residues were dried in an oven at 40°C. For each sample, approximately 300 specimens of benthic foraminifera larger than 63 μm were picked and mounted on microslides for permanent record.

We performed a morphogroup analysis to infer probable microhabitat preferences of benthic foraminifera as well as environmental conditions at the seafloor (nutrient availability, bottom-water oxygen, and seasonality) (e.g., Bernhard, 1986; Fontanier et al., 2002; Jorissen et al., 1995). Species were grouped additionally according to their particular paleoecological affinities: suboxic-dysoxic taxa (Bernhard, 1986; Kaiho, 1991), opportunistic species (Boscolo-Galazzo et al., 2015; Dias et al., 2018; Eichler et al., 2019; Erbacher et al., 1999; Fontanier et al., 2002; Hayward et al., 2005; Smart et al., 1994), and phytodetritus exploiting taxa (PET) (Gooday, 1988, 1993; Jorissen et al., 2007; Suhr et al., 2003) (Table S4).

The diversity of the assemblages (Fisher-α, Fisher et al., 1943) and the percentage of agglutinated and calcareous taxa were calculated. Benthic foraminiferal accumulation rates (BFAR) were calculated using the equation proposed by Herguera and Berger (1991):

$$\mathrm{BFAR} = (\mathrm{nr/gr} > 63\,\mu\mathrm{m} * \%\mathrm{wt} > 63/100) * \mathrm{LSR} * \mathrm{DBD}$$

$$\mathrm{CFAR} = \%\mathrm{wt} > 63\,\mu\mathrm{m} * \mathrm{LSR} * \mathrm{DBD}$$

where BFAR is expressed as counts cm^{-2} kyr^{-1}: nr/gr >63 μm is the number of benthic foraminifera per gram of sediment from the >63 μm size fraction; %wt > 63 μm is the weight percentage of the >63 μm size fraction; LSR is the linear sedimentation rate (cm/kyr), and DBD is the dry bulk density (g cm^{-3}). The latter was interpolated from measurements of moisture and density (MAD) samples taken during Expedition 371 (Sutherland et al., 2019). The coarse fraction accumulation rate (CFAR) was determined by multiplying the %wt >63 μm size fraction by the LSR and the DBD. The CFAR often can be a proxy for current strength as well as an approximation of planktonic foraminiferal accumulation rates (Diester-Haass, 1995).

Multivariate analyses on the relative abundance of benthic foraminiferal taxa were performed using PAST software v. 3.04 (Hammer et al., 2001), as a tool to evaluate the response of benthic foraminiferal assemblages to environmental changes. These analyses were based on a data set of species with a relative abundance >5% in at least one sample, the unweighted pair-group average algorithm (UPGMA) and the Pearson correlation were used as similarity coefficients. A hierarchical cluster analysis of species (n = 20) (Figure S2 in Supporting Information S1; Table S3), and Detrended Correspondence Analyses (DCA) in R-mode (species; Figure S3 in Supporting Information S1), and Q-mode (samples; Figure S4 in Supporting Information S1) were carried out on the same data set to investigate the environmental variables that may have controlled the distribution patterns of benthic foraminifera.

Species-specific stable isotopes ($\delta^{13}C$) were analyzed on 221 collections of *Cibicidoides mundulus* from samples between 221.75 and 85.31 m (Table S6), and on 161 collections of *Trilobatus sacculifer* from samples between 221.77 and 82.41 m CSF-A, using standard procedures (Text S3 in Supporting Information S1).

3. The Late Miocene-Early Pliocene at Site U1506

3.1. Calcareous Nannofossil Biostratigraphy

Calcareous nannofossils are commonly abundant and moderately well-preserved across all the samples. Generally, taxonomic identification can be made at the species level. Despite the low abundance and sporadic occurrence of some taxa, we were able to apply the adopted biozonations performing counts on 2 mm^2, which were then normalized to the standard area of 1 mm^2 proposed by Backman and Shackleton (1983). The selected biohorizons are listed in stratigraphic order in Table 1. In summary, the studied interval spans from 7.4 to 4.5 Ma,

Table 1
Biohorizons Used to Biostratigraphically Classify the Studied Succession

Event	Species	Biozone Okada and Bukry (1980)	Biozone Martini (1971)	Biozone Backman et al. (2012)	Depth (CSF-A) top	Depth (CSF-A) bottom	Depth (CSF-A) midpoint	Depth error (m)	Sample top	Sample base	Age (Ma) Backman et al. (2012)
T	*Discoaster quinqueramus*	CN10	NN23	CNM20	123.01	126.00	124.51	1.49	IODP-U1506A-14R-3W, 71 cm	IODP-U1506A-14R-5W, 70 cm	5.59
T	*Nickilithus amplificus*			CNM19	153.26	154.92	154.09	0.83	IODP-U1506A-17R-4W, 76 cm	IODP-U1506A-17R-CC, 05 cm	5.94
B	*Nickilithus amplificus*			CNM18	154.92	159.85	157.39	2.47	IODP-U1506A-17R-CC, 05 cm	IODP-U1506A-18R-2W, 75 cm	6.91
B	*Amaurolithus primus*	CN9b		CNM17	222.97	223.23	223.10	0.13	IODP-U1506A-24R-6W, 37 cm	IODP-U1506A-24R-CC, 05 cm	7.42
B	*Discoaster berggrenii*	CN9a		CNM16	228.45	229.95	229.20	0.75	IODP-U1506A-25R-3W, 75 cm	IODP-U1506A-25R-4W, 75 cm	8.29
B	*Discoaster quinqueramus*		NN11		229.95	232.95	231.45	1.50	IODP-U1506A-25R-4W, 75 cm	IODP-U1506A-25R-6W, 75 cm	8.11

Note. From left to right: type of event (T, top; B, base), species and the relative biozones they define (Backman et al., 2012; Martini, 1971; Okada & Bukry, 1980), samples and their depths, and the age associated to each biohorizon (Backman et al., 2012).

from Zone NN10 to Zone NN12 (Martini, 1971), Subzone CN8b to Subzone CN10 (Okada & Bukry, 1980), and Zone CNM15 to Zone CNM20 (Backman et al., 2012) (Figure S1 in Supporting Information S1).

3.2. Carbon Stable Isotopes

The analyses of *C. mundulus* ($\delta^{13}C_{benthic}$) cover ca. 3 Myr of deposition, from 7.4 to 4.6 Ma. Across this time interval, $\delta^{13}C_{benthic}$ ranges between 0.06 and 1.37‰ (Figure 3a). The $\delta^{13}C_{benthic}$ record displays an initial decrease in values between 7.4 and 6.8 Ma, followed by an increase between 0.6 and 1.37‰ until 5.9 Ma when the trend changes. Two marked $\delta^{13}C_{benthic}$ minima are observed at 5.9 Ma (0.06‰) and 4.9 Ma (0.16‰). Although the $\delta^{13}C_{benthic}$ data have a lower sampling resolution in the upper part of the record, a 1.01‰ increase is observed between 5.9 and 5.5 Ma, preceding a decline of −0.91‰ in 0.6 Myr, between 5.5 and 4.9 Ma.

The planktonic foraminiferal $\delta^{13}C$ record ($\delta^{13}C_{plank}$; *T. sacculifer*) ranges between 1.06 and 2.80‰ throughout the study interval (Figure 3b). The record exhibits gradually decreasing $\delta^{13}C_{plank}$ values from the older to younger sediment, but with three stepped declines. The first and most prominent drop occurs at ca. 6.8 Ma, where a 0.97‰ decrease in $\delta^{13}C_{plank}$ happened within 60 kyr. The second drop occurred at ca. 6.05 Ma, where $\delta^{13}C_{plank}$ shows a decrease of 0.92‰ in 150 kyr, and the last $\delta^{13}C_{plank}$ decline takes place at ca. 5.5 Ma, with a decline of 0.83‰ in 90 kyr. From 5.3 until 4.5 Ma the record shows an overall decrease and low values, in this interval the average $\delta^{13}C_{plank}$ values decline to ca. 1.87‰.

From the benthic and planktonic foraminiferal $\delta^{13}C$ records, we calculated the vertical $\delta^{13}C$ gradient at Site U1506 (Figure 3c). The $\Delta\delta^{13}C$ (planktonic-benthic) ranges between 1.02‰ and 2.00‰ with the minimum and maximum at 4.9 Ma and 6.8 Ma, respectively. The record shows an initial increase in $\delta^{13}C$ values of ca. 0.90‰ between 7.4 and 6.8 Ma, followed by a decrease toward the end of the studied interval. A shift towards more positive values is present at ca. 6.1 Ma, where the record shows a positive peak (1.99‰). The average value of the entire record is 1.52‰, similar to that calculated in the 7.4–6.8 Ma interval, and the values decrease to 1.24‰ between 5.5 and 4.5 Ma.

The $\delta^{13}C$ datasets have been compared to those generated at IODP Site U1338 in the Eastern Equatorial Pacific Ocean (Drury, Lee, et al., 2018; Drury, Westerhold, et al., 2018; Drury et al., 2016) to strengthen our age model, to date with precision all the observed changes (Figure 3), and to distinguish the regional and global components of the isotopic signal. Stable isotopes analyses at Site U1506 have been carried out on the same planktonic and benthic species used in Drury et al. (2016); Drury, Lee, et al. (2018), Drury, Westerhold, et al. (2018).

There is an offset of ca. 1‰ between the two $\delta^{13}C$ records of *C. mundulus*, Site U1338 $\delta^{13}C_{benthic}$ ranges between −1.48 and 0.73‰, while Site U1506 shows more positive values (0.06–1.37‰). The $\delta^{13}C$ records of *T. sacculifer* from Site U1506 and U1338 exhibit similar overall long-term (million-year) trends. The planktonic record ranges between 1.06‰ and 2.80‰ at Site U1506, and between 1.08‰ and 2.53‰ at Site U1338. Both records show decreasing $\delta^{13}C_{plank}$ values towards the younger ages, but the most negative $\delta^{13}C_{plank}$ value is located at 5.0 Ma (1.06‰) at Site U1506, and 7.01 Ma at Site U1338. This offset is likely due to the different water masses that bathe the two sites. Site U1338 is at 4,200 m water depth and bathed by deep water masses, while Site U1506 (1,505 m water depth) is bathed by intermediate water masses. Despite the offset and the lower resolution of Site U1506, the records show a very similar long-term trend.

3.3. Integrated Age Model and Sedimentation Rates

We refined the shipboard biostratigraphic age-control by compiling a higher resolution calcareous nannofossil biostratigraphy (Table 1). The obtained biochronology is in good

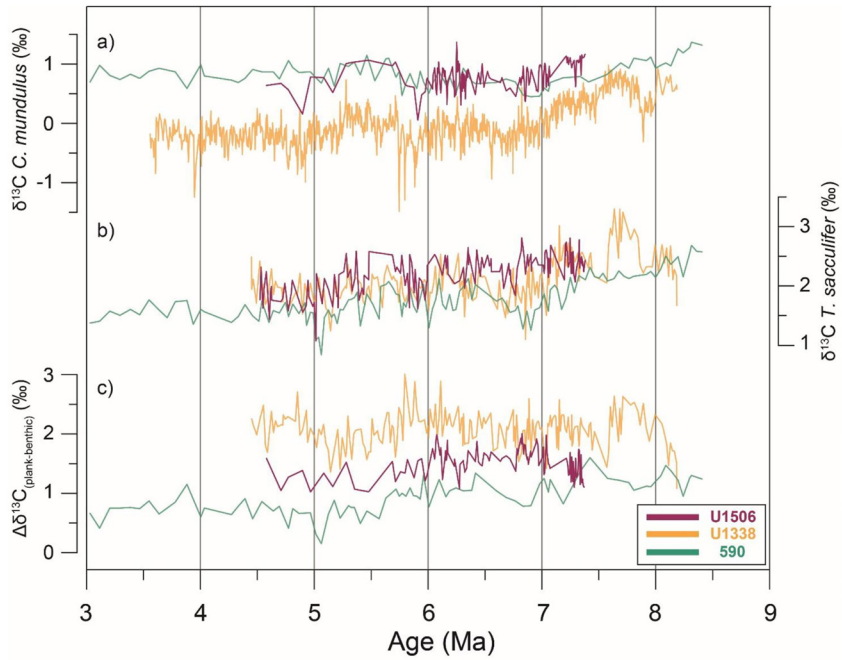

Figure 3. Stable carbon isotope records at IODP Site U1506 (this study), IODP Site U1338 (Drury et al., 2016; Drury, Lee, et al., 2018, Drury, Westerhold, et al., 2018) and ODP Site 590 (Elmstrom & Kennett, 1986; Grant & Dickens, 2002) plotted against age (Ma).

agreement with the age model of Sutherland et al. (2019), and allows for an implementation of the tuned age model from Cores U1506-10R to 25R (Figure 4; Table S7). We refined the age model for Site U1506 for the sediment interval spanning from 7.4 to 4.2 Ma based on orbital tuning of the Natural Gamma Radiation (NGR) and color reflectance shipboard data (Sutherland et al., 2019) to the daily insolation at 65°N on 21st June (summer) from the Laskar 2004 orbital solution (Laskar et al., 2004).

Before the tuning process, we investigated the phase relationship between the data and the target curve. More positive benthic foraminifera oxygen isotope values correlate with higher XRF core scanning iron (Fe) and silica (Si) elemental abundance values (Table S9), higher NGR, and lower color reflectance a* values (red/green ratio) in Core 19R (Figure S6 in Supporting Information S1). Benthic foraminifer oxygen isotope values are higher within minima in summer insolation at 65°N, which correspond to glacial periods. Assuming that the phase relationship is constant, NGR maxima should correspond to daily summer insolation minima at 65°N. To test if and which astronomically driven cycles are present in the NGR and reflectance data of Site U1506, spectral analysis in the depth domain was carried out (Figure S7 in Supporting Information S1).

The updated sedimentation rates show that the dominant cycles occur with a frequency of ~1.1 cycles/meter (~90 cm-long cycles; Figure S7 in Supporting Information S1), and relate to precession cycles. Longer cycles on the order of ~0.2 cycles/meter (5 m-long cycles) relate to short eccentricity. Using the biostratigraphy as a starting point, prominent NGR maxima then were tuned to minima in summer insolation at 65°N on 21st June (Figure 5; Figure S8 in Supporting Information S1). We extrapolated the ages for the base (221.75 m CSF-A) and top (82.01 m CSF-A) of our studied interval to 7.4 and 4.5 Ma.

We compared the pattern in the benthic stable carbon isotope record of Site U1506 to the Cenozoic Global Reference benthic foraminifer carbon and oxygen Isotope Data set (CENOGRID; Figure S5 in Supporting Information S1) (Westerhold et al., 2020), and from the good agreement, we conclude that a robust astrochronology has been developed for Site U1506, even though the hole was rotary drilled.

Linear sedimentation rates were calculated based on the bio-astrochronological age model, from 7.4 to 6 Ma LSRs values are around 4.7 cm/kyr, then increase up section to a maximum of 7.6 cm/kyr at 6.7 Ma. Between 6.6 Ma and the top of the interval at 4.5 Ma, LSRs show a slight decrease but with values still high, around 5.0 cm/kyr, showing an abrupt decrease after 3 Ma. The shipboard results show that calcium carbonate content

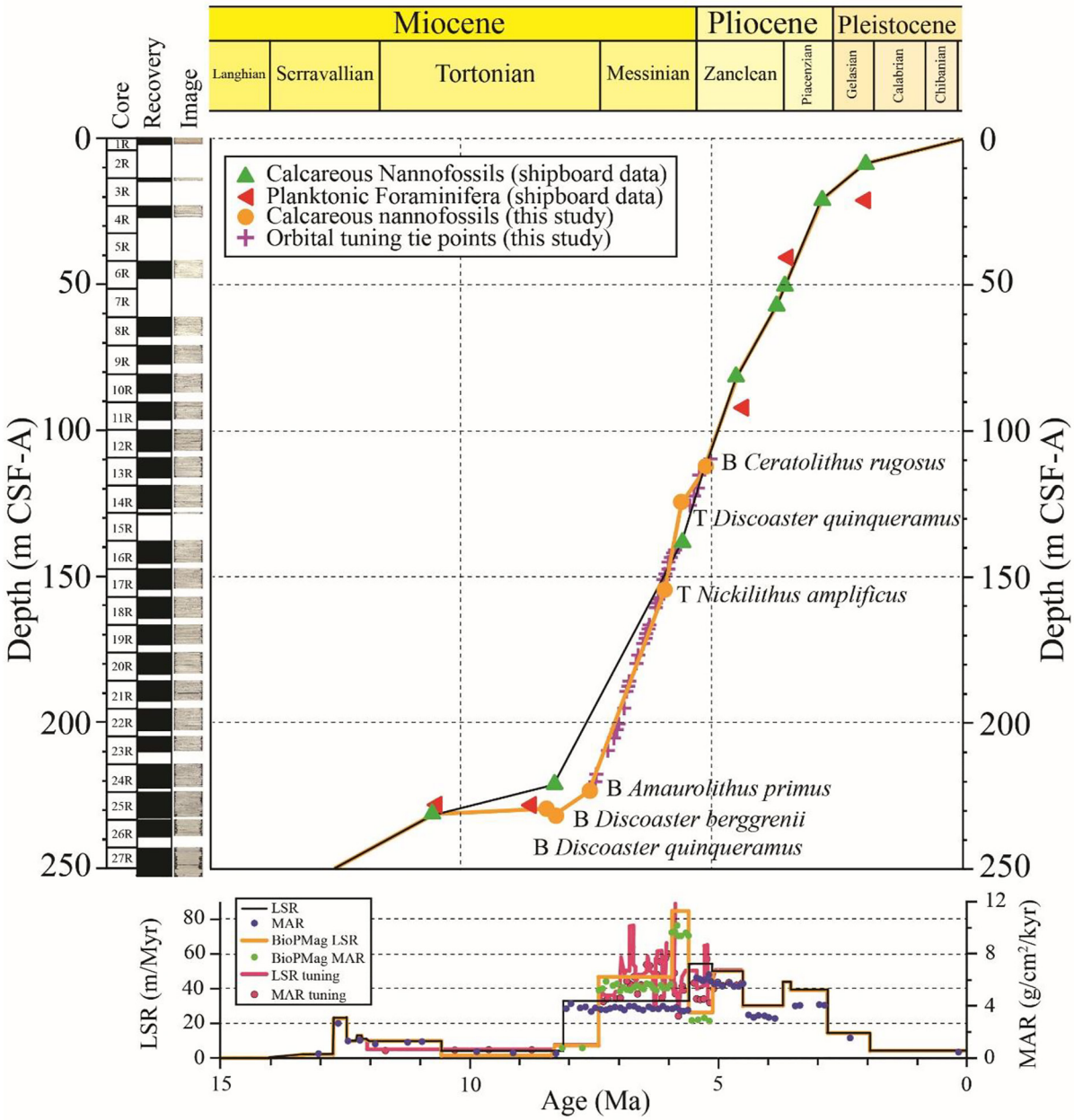

Figure 4. Age model and sediment accumulation rates over time at IODP Site U1506. Black line: shipboard age model; Orange line: this study. Left: core recovery and image. Bottom: compacted linear sedimentation rates and total mass accumulation rate. Orange circles are new calcareous nannofossil data from this study (modified after Sutherland et al., 2019).

varies between 88 and 95 wt% and generally increases with depth, with the highest values between 200 and 228 m (Sutherland et al., 2019). Carbonate contents were derived by linear interpolation from the shipboard data between Core 27R and Core 1R (247.18–0 m) and used to calculate the carbonate mass accumulation rates (MAR_{Carb}) for each sample according to:

$$MAR_{Carb} = \%wt\ CaCO_3 * LSR * DBD$$

MAR_{Carb} is expressed as (g cm^{-2} kyr^{-1}), LSR is the linear sedimentation rate (cm/kyr) calculated from the age model and DBD is the dry bulk density (g/cm^3). The DBD was interpolated from the MAD samples and the data were normalized using the Z-score Normalization in Excel (Table S8). MAR_{Carb} older than 7.4 Ma have values

10.1029/2022PA004565

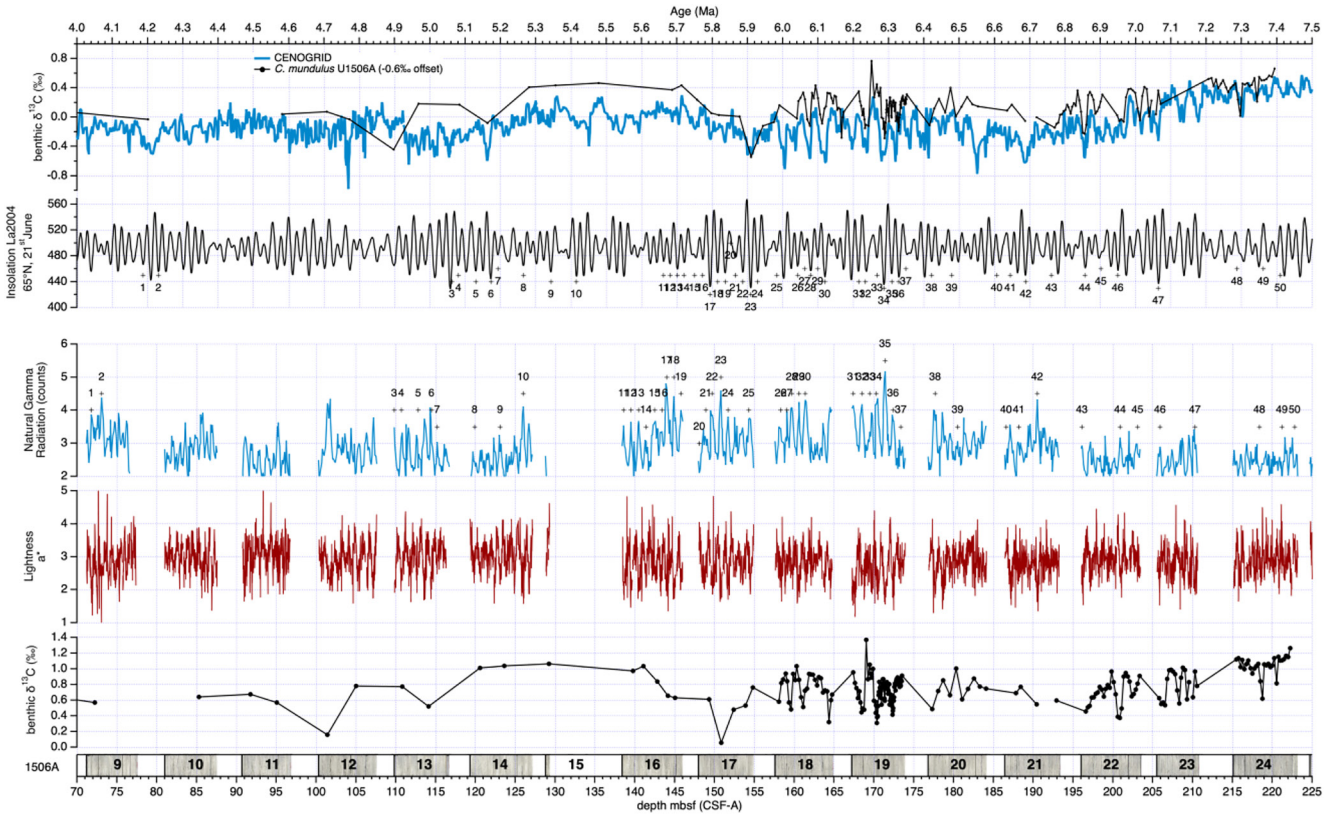

Figure 5. Detailed plot of tuning strategy spanning from U1506A Core 9R to Core 24R. Given are the core images, benthic stable carbon isotope data (this study), lightness a* values, and Natural Gamma Radiation (NGR) data (both shipboard) versus depth. In the upper part plotted is the 65° North insolation at 21st of June (Laskar et al., 2004), the CENOGRID carbon isotope record (Westerhold et al., 2020), and the U1506A carbon isotope data versus age. The numbers mark the tie-points between NGR data and the insolation target curve.

between 0.5 and 1 g cm^{-2} kyr^{-1}, and values increase up-hole to reach a maximum at 6.7 Ma (8.21 g cm^{-2} kyr^{-1}). Between 6.7 and 4.5 Ma, MAR_{Carb} varies between 4 and 8 g cm^{-2} kyr^{-1}, then drop below 4 g cm^{-2} kyr^{-1} in sediments younger than 4.5 Ma.

3.4. Paleoenvironment: Benthic Foraminiferal Assemblages

Benthic foraminifera are well preserved and strongly dominated by calcareous and infaunal taxa such as *Bulimina*, *Globocassidulina*, or *Uvigerina* (Table S2). Assemblages are diverse, and Fisher-α values (Alegret et al., 2021) range between 20.8 and 33.2, with higher values (>27.9) between 192.91 and 150.84 m CSF-A (Figure 6). Species with similar paleoecological affinities were placed into three groups: suboxic-dysoxic taxa, opportunistic species, and PET (Table S2). Suboxic-dysoxic taxa make up between 22% and 59% of the assemblages, with minimum values in the lower part of the study interval. Opportunistic taxa make up 10%–56% of the assemblages, and the abundance of PET taxa ranges between 2.59% and 40.33%. Both opportunistic taxa and PET show high relative abundance in the lower part of the study interval and a secondary peak between 4.9 and 4.8 Ma (from 101.41 to 95.05 m CSF-A; Figure 6). Benthic foraminiferal accumulation rates (BFAR) show an upward decreasing trend, and the coarse fraction (>63 μm) accumulation rates (CFAR) show overall high values and an upward decreasing trend between 7.4 and 5.8 Ma (from 221.75 to 144.17 m CSF-A), followed by another increase that peaks at 4.5 Ma (82.01 m CSF-A; Figure 6).

In the R-mode DCA analysis (Figure S3 in Supporting Information S1), species are grouped into four subclusters that are also differentiated in the hierarchical cluster analysis (Figure S2 in Supporting Information S1). Among other species, Cluster A includes various representatives of the genera *Cibicidoides* and *Uvigerina*. Subcluster A1 falls within low values along both Axis 1 and Axis 2, while Subcluster A2 dominates at high values along Axis 2. Subcluster B1 (*Bulimina elongata*, *Ehrenbergina carinata*, *Oridorsalis umbonatus*) falls in intermediate values

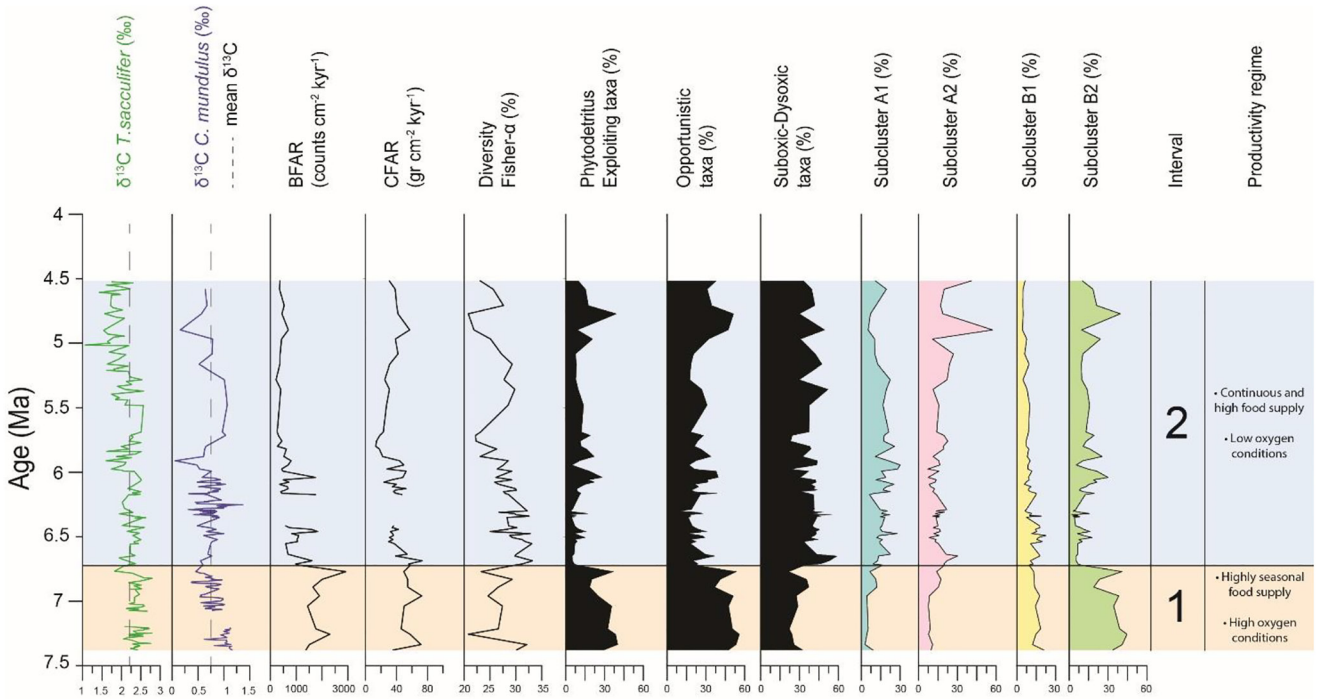

Figure 6. Benthic and planktonic stable carbon isotope records, BFAR, CFAR, diversity (Fisher-α index), relative abundance of phytodetritus exploiting taxa, opportunistic taxa, suboxic-dysoxic taxa, and subclusters plotted against age (Ma). Highlighted Interval 1 (orange), Interval 2 (blue) indicate the productivity regimes.

along Axis 1 and low values in Axis 2. Subcluster B2 includes PET taxa such as *Epistominella exigua*, *Globocassidulina crassa*, and *Globocassidulina subglobosa*, and it shows high values along Axis 1 and low values along Axis 2. Axis 1 is likely related to continuity of the food supply, with more continuous food supply at low values and more pulsed food input towards higher values along this axis. The disparity in distribution does not allow for an accurate interpretation of Axis 2, as species are generally clustered horizontally and have less variable vertical spread, except for *Cibicidoides wuellestorfi* and *Spiroplectammina spectabilis*. The quantitative and statistical analyses of the assemblages allowed for differentiation of two intervals with paleoenvironmental significance.

Interval 1 spans from 7.4 to 6.7 Ma (from 221.75 to 194.75 m CSF-A; Figure 6) and is characterized by a high abundance of Subcluster B2, high BFAR values, small-sized benthic foraminifera, and high percentages of PET (e.g., *E. exigua*, *G. crassa*) and opportunistic taxa (e.g., *G. subglobosa*, *Osangularia culter*). High abundance of PET has been related to pulsed seasonal delivery of phytodetritus to the seafloor (Boscolo-Galazzo et al., 2015; De Almeida et al., 2015) and probably to an opportunistic life strategy and rapid reproduction, which is consistent with the small-sized benthic foraminifera observed in this interval. Since PET reproduce rapidly and build large populations, such rapid increases in population size likely lead to increased test counts per gram of sediment, which may account for the high BFAR values in this interval (Smart et al., 2007). Corliss et al. (2009) speculated that these abundance peaks, and the consequent rapid flux of organic carbon to the seafloor, are the results of changes in the environmental conditions in the upper part of the water column. The transport of phytodetritus to the ocean floor could then explain the rapid proliferation of small, opportunistic taxa (Gooday, 2002).

The lowermost diversity values are recorded in Interval 1, as expected for an interval with abundant opportunist taxa (e.g., Murray, 2006). Seasonal food input and low abundance of dysoxic taxa point to well-oxygenated bottom waters, likely related to an intensified current strength. This is further supported by high CFAR and a high abundance of *G. subglobosa* and *G. crassa*, which are common in areas with high current activity (Schmiedl et al., 1997). This hypothesis is also in agreement with the low percentage of suboxic-dysoxic taxa and with the interpretation of Axis 1 of the DCA R-mode (species) plot.

All these observations and the relatively low values of $\delta^{13}C_{benthic}$ during Interval 1 point to high productivity, and the combination of high BFAR, small specimens, and peaks in PET and opportunistic taxa possibly indicate a high seasonal surface primary productivity by phytoplankton blooms.

Interval 2 spans from 6.7 to 4.5 Ma (from 194.75 to 82.01 m CSF-A; Figure 6) and is dominated by infaunal morphogroups and thin-walled suboxic-dysoxic indicators (e.g., *Bolivina*, *Bulimina*, *Chilostomella*, *Fursenkoina*, *Uvigerina* species; Kaiho, 1994) that indicate high productivity. Subcluster A1 dominates from 6.7 to 5.1 Ma (from 194.75 to 110.81 m CSF-A), and its main components (*Bulimina truncana*, and *Uvigerina proboscidea)* consist of infaunal species that are linked to high productivity conditions and low oxygen levels. In the R-mode (species) DCA, Subcluster A1 falls at low values along Axis 1, indicating a continuous high food supply to the seafloor. Between 5.1 and 4.5 Ma (from 110.81 to 82.01 m CSF-A), Subclusters A2 and B2 dominate the interval with high percentages of *S. spectabilis* and *G. crassa*, which coincide with peaks in both PET and opportunistic species, pointing to a short phase of high productivity likely driven by phytoplankton blooms. Overall, Interval 2 is characterized by abundant "high-productivity taxa" such as *Bolivina*, *Bulimina*, *Melonis*, and *Uvigerina* (Smart et al., 2007). Diversity oscillates during this interval and normal-sized benthic foraminifera have been observed, in contrast to the small-sized specimens from Interval 1. Suboxic-dysoxic species also dominate this interval showing an increased abundance from 6.7 Ma upward.

The BFAR shows a decreasing trend and low values until 4.5 Ma, which is inconsistent with the interpreted high productivity conditions, however, the interpretation of BFAR as a paleoproductivity proxy in low oxygen environments is not always straightforward (Naidu & Malmgren, 1995). Productivity was high during Interval 2, but in contrast to Interval 1, the dominance of low oxygen foraminiferal taxa indicates a continuous and high food supply to the seafloor and oxygen deficiency during Interval 2. These conditions were probably associated with a decrease in current strength, supported by the decrease in CFAR during this interval.

4. Disentangling the Biogenic Bloom: Insights From the Tasman Sea

4.1. Biogenic Bloom Basics Beyond and Within the Tasman Sea

Increases in MAR_{Carb} and changes in benthic foraminiferal assemblages mark the Biogenic Bloom at numerous locations. Examples from locations in the Atlantic, Indian and Pacific highlight these basic observations.

In the Atlantic Ocean, reconstructions at Sites 982, 925, and 1088 show increased MAR_{Carb} and food supply to the benthos between 8.2 and 5.4 Ma, with peaks between ca. 6.4 and 6.0 Ma (Diester-Haass et al., 2005). At ODP Sites 1085, 1086 and 1087, Diester-Haass et al. (2004) identified the Biogenic Bloom based on MAR_{Carb} and total organic carbon mass accumulation rates and inferred a sharp increase in paleoproductivity using BFAR and *Uvigerina* counts at ca. 6.7 Ma, associated with increased MAR_{Carb}. Drury et al. (2021) produced an astronomicallytuned record of the Biogenic Bloom at ODP Site 1264, and identified high MAR_{Carb} between ca. 7.8 and 3.3 Ma, with peak values between 7.2 and 6.6 Ma.

In the Indian Ocean, Dickens and Owen (1999) summarized previous work at ODP Sites to suggest high MAR_{Carb} at multiple locations between 9 and 3.5 Ma, with a general maximum between 6.0 and 5.0 Ma. A contemporaneous expansion of the intermediate water oxygen minimum zone (OMZ) is evidenced at several sites from a decrease in Mn/Sc ratio (Dickens & Owen, 1994) or benthic foraminifera assemblages dominated by *Bolivina* spp. and *Uvigerina* spp. (Hermelin, 1992). Benthic assemblages from ODP Site 752 point to oxygen deficiency and high variability (in productivity or changes in ocean currents) between 9 and 4.5 Ma (Singh et al., 2012).

The Biogenic Bloom was first emphasized in summaries of results from DSDP and ODP drill sites in the Eastern Equatorial Pacific (EEP), whereby elevated MAR_{Carb} characterized upper Miocene-lower Pliocene sediment (Farrell et al., 1995; Van Andel et al., 1975). Since this recognition, six astronomically tuned sites in this region provide refined timing: the high MAR_{Carb} fingerprint manifests between ~8 and 4.4 Ma, with a peak at ca. 7 Ma (Lyle et al., 2019). At another orbitally tuned site, ODP Site 846, Diester-Haass et al. (2006) documented concurrent peaks in MAR_{Carb} and BFAR at 7.4 , 6.4, 5.6, and 4.9 Ma, with a paleoproductivity reconstruction using BFAR and elemental ratios that points to enhanced productivity between 6.4 and 4.5 Ma. In the far north Pacific, sediment mass accumulation rates peak between 8.1 and 3.5 Ma (Dickens & Owen, 1999; Rea et al., 1995), but this is mostly caused by excess diatom burial.

Previous research within the Tasman Sea identified the Biogenic Bloom at ODP Site 1172, located on the East Tasman Plateau (Diester-Haass et al., 2006), and at Deep Sea Drilling Project (DSDP) Site 590 (Grant & Dickens, 2002) and Sites U1506, U1508 and U1510 on the LHR (Sutherland et al., 2022, Figure 2). At Site 1172, MAR_{Carb} peaks at 7 and 5.5 Ma and paleoproductivity based on the BFAR shows two peaks, at ca. 7.2 and after

6.0 Ma. *Uvigerina* becomes more abundant during these paleoproductivity peaks, indicating an enhanced flux of organic matter to the seafloor. At DSDP Site 590, there is evidence for elevated primary productivity between 9 and 3.8 Ma; however, MAR_{Carb} peaks at 5 Ma, while elemental ratios (Ca/Ti, Ba/Ti, and Al/Ti) peak at 6.5 Ma. A 2 Myr offset was documented between $\delta^{13}C$ records of bulk sediment and surface-dwelling planktonic foraminifera (both showing a similar ca. 1 ‰ decrease), possibly due to variations in the composition and depth habitats of coccolithophorids, and alterations in the upwelling rate at the Tasman Front (Grant & Dickens, 2002).

At Site U1506, MAR_{Carb} display high values throughout the investigated interval (ca. 5–7 g cm^{-2} kyr^{-1} between 7.4 and 4.5 Ma) with a peak at ca. 6.7 Ma (ca. 8.5 g cm^{-2} kyr^{-1}), and benthic foraminifera and stable carbon isotopes point to increased paleoproductivity between 7.4 and 4.5 Ma. Our integrated data set, provides a new astronomically constrained record of part of the Biogenic Bloom in the Tasman Sea, spanning from 7.4 to 4.5 Ma. The accuracy of the implemented age model, and consequently of the LSRs, is supported by the general consistency with the CENOGRID carbon isotope record (Figure S5 in Supporting Information S1, Westerhold et al., 2020) and by the high correlation of $\delta^{13}C$ values between Sites U1506 and U1338 (Drury et al., 2016; Drury, Lee, et al., 2018; Drury, Westerhold et al., 2018).

Most studied locations in the Tasman Sea show evidence of the Biogenic Bloom, yet no clear and uniform pattern emerges for the region. The three sites highlighted here show asynchronous MAR_{Carb} peaks (Figure 7b), and the apparent diversity in the proxy records for increased sediment accumulation and productivity from the Tasman Sea emphasizes the role of local and regional conditions. The complex system of eddies and gyres of the Tasman Front, the local topography, and the strong current activity inferred from benthic foraminifera could account for the differences in MAR_{Carb} peaks. Variability between the datasets of the Tasman Sea sites could also originate from the age control, as Site U1506 is the only one with an astronomically tuned age model, while Sites 1172 and 590 have a biostratigraphic and paleomagnetic age control. In the next sections, we compare the new productivity data from Site U1506 with other records of the Biogenic Bloom to explore how local, regional and global processes influenced the expression of the Biogenic Bloom in the Tasman Sea.

4.2. Diverse Expression of the Biogenic Bloom on Lord Howe Rise

If carbonate dissolution was minimal, which seems likely at the relatively shallow depths of LHR (1,000–3,000 m), changes in MAR can be used to evaluate changes in surface water productivity and to infer the presence of the Biogenic Bloom. Data from Sites 590 and U1506 confirm elevated primary productivity associated with the Biogenic Bloom during the Late Miocene-Early Pliocene. We quantitatively compare MAR_{Carb} at Site U1506 and 590 (Grant & Dickens, 2002) with the broader Tasman Sea region (Sutherland et al., 2022). There is a general MAR peak in the Tasman Sea at around 5 Ma (Figure 7b), and this is observed at Site 590 between 5 and 4.3 Ma. A second peak at 8 to 6 Ma is documented for northern LHR and northern New Caledonia Trough, but this second peak is not present at Site 590 (Figure 7b) and is not synchronous with high MAR_{Carb} documented between 7 and 6 Ma at Site U1506. The asynchrony between the U1506 data and other datasets could either be the result of different datums used to construct age models, local settings, or lower resolution of other age models, or it could be a real difference in MAR_{Carb} between sites.

Integrating MAR_{Carb} with other paleoproductivity proxies allows us to have a deeper understanding of the Biogenic Bloom. We compared planktonic and benthic $\delta^{13}C$ records from Sites U1506 and 590 (Elmstrom & Kennett, 1986; Grant & Dickens, 2002). They show similar overall trends. The most notable difference is found in the planktonic record between 7.4 and 6.7 Ma. Site U1506 shows positive and increasing values that could be interpreted in terms of higher surface productivity by phytoplankton primary producers, while $\delta^{13}C$ values display a decreasing trend at Site 590.

The interval between 7.4 and 6.7 Ma corresponds to the final stage of the Late Miocene Carbon Isotope Shift (LMCIS; e.g., Hodell & Venz-Curtis, 2006; Drury et al., 2017). Site 590 shows a large stepped change in planktonic $\delta^{13}C$ between 8 and 6.5 Ma, which is consistent with other global records (Figure 7c). A similar shape of planktonic and benthic $\delta^{13}C$ records during the LMCIS is documented at Site U1338 (in the EEP). The variation in $\delta^{13}C$ observed over time typically results from a carbon partitioning between organic and carbonate reservoirs (e.g., Berner, 1990; Kump & Arthur, 1999; Vincent et al., 1980). The scenario proposed for this relatively long-term shift is likely a signal of a global shift in the oceanic $\delta^{13}C$ reservoir rather than related to a shift in productivity *tout court* (Drury, Lee, et al., 2018; Drury, Westerhold, et al., 2018). The LMCIS is partially blurred by the

10.1029/2022PA004565

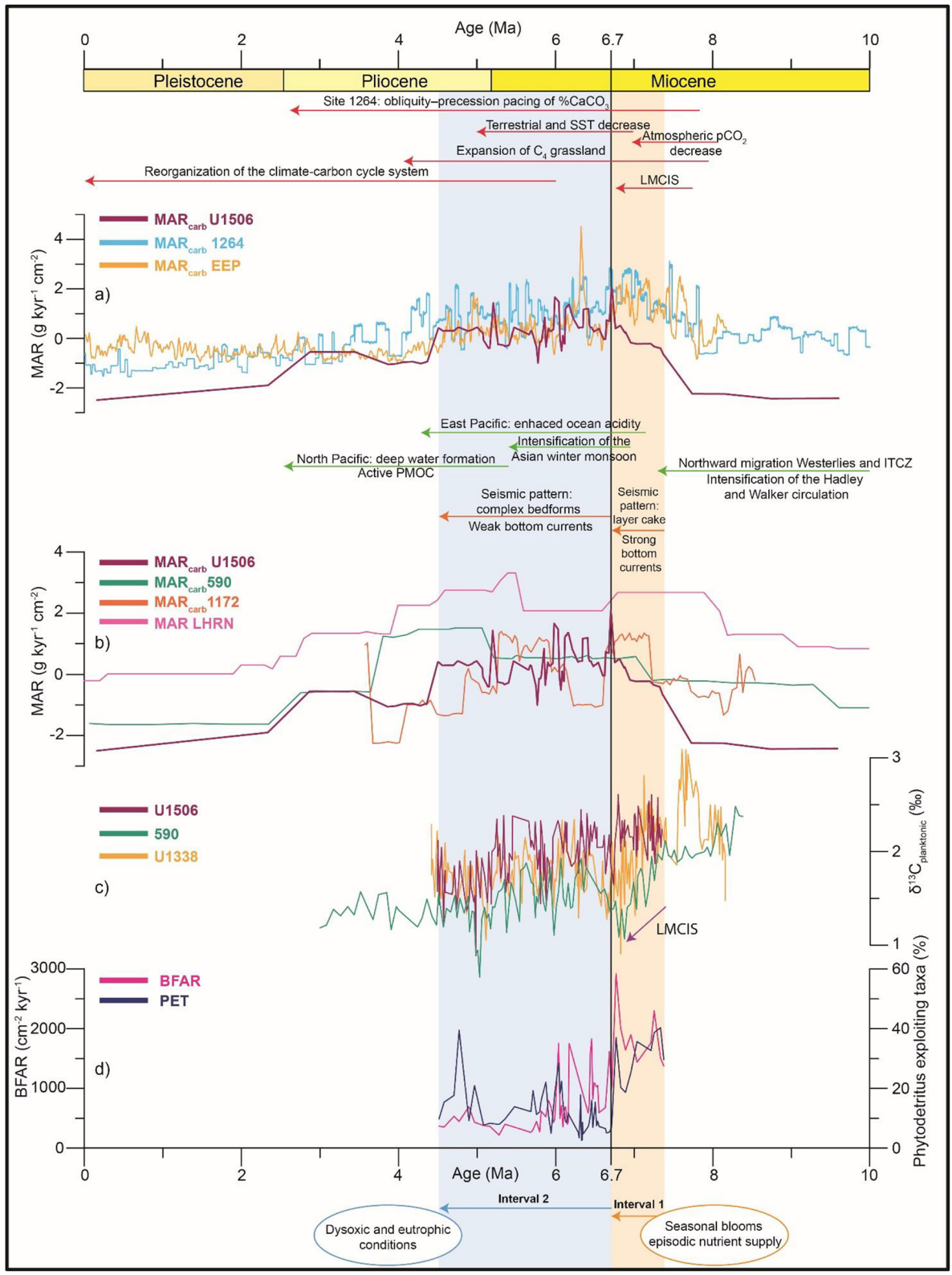

Figure 7. Local (orange arrows), regional (green arrows), and global (red arrows) events during the Late Miocene-Early Pliocene. (a) Normalized MAR_{Carb} of Site U1506 (purple), 1264 (light blue) and EEP (yellow); (b) normalized MAR_{Carb} of Site U1506 (purple), 590 (green) (Grant & Dickens, 2002), 1172 (orange) (Diester-Haass et al., 2006), and MAR of Northern Lord Howe Rise (pink) (LHRN, Sutherland et al., 2022); (c) planktonic $\delta^{13}C$ of Site U1506 (purple), Site U1338 (yellow) and 590 (green) (Grant & Dickens, 2002); Site U1506 BFAR (pink) and relative abundance of phytodetritus exploiting taxa (dark blue).

local productivity signal at Site 590, but the $\delta^{13}C$ planktonic record mostly reflects global seawater $\delta^{13}C$ changes with only a minor influence due to local productivity changes. At Site U1506 the general decline in $\delta^{13}C$ is not observed, with values increasing up-section or, at least remaining stable with high-amplitude short-term fluctuations. We suggest that the LMCIS imprint at Site U1506 was overwhelmed by the local productivity signal. Between 6.5 and 5 Ma, the planktonic to benthic $\Delta\delta^{13}C$ at Site 590 and U1506 decreased (Figure 3c). Grant and Dickens (2002) suggested this could either indicate a decrease in surface water productivity or a reduction in water column density stratification. This $\Delta\delta^{13}C$ decrease is not present at Site U1338 (Figure 3c), and it could indicate that Sites 590 and U1506 were more heavily influenced by local productivity signals after the LMCIS.

Grant and Dickens (2002) suggested that divergence in the $\delta^{13}C$ of different biogenic carbonate phases observed at Site 590 could be related to changes in water mass structure. Differences observed in MAR_{Carb} and $\delta^{13}C$ between Sites U1506 and 590 are possibly related to the complexity of the local oceanography, specifically the interactions between the Tasman Front, intermediate waters, and topography of LHR.

4.3. Regional Impact of the Biogenic Bloom Signal in the Tasman Sea

The Biogenic Bloom can be traced from LHR to other sites in the Tasman Sea. Sutherland et al. (2022) reported elevated MAR values between ca. 9 and 4 Ma in 11 boreholes, from LHR to Reinga Basin and New Caledonia Trough. MAR data from the northern LHR (Sutherland et al., 2022) are continuous and have high values but local peaks in MAR do not always correlate well between sites. Between 7.4 and 4.5 Ma, MAR_{Carb} at Site U1506 show an articulated pattern, and this is also reflected in benthic foraminiferal data. Our results from Site U1506 indicate a significant local paleoceanographic change at 6.7 Ma, from seasonal food supply in the form of phytodetritus, to more continuous high productivity associated with less intense bottom water currents.

The change in productivity regime observed at 6.7 Ma at Site U1506 coincides with a prominent stratigraphic change identified on seismic profiles, switching from complex bedform beneath, to a more layer-cake pattern above (Figure 2; Sutherland et al., 2022). This change in bedform geometry is consistent with a local reduction in bottom current strength after 6.7 Ma. Benthic foraminifera and CFAR suggest strong bottom currents in Interval 1 (Figure 6). In contrast, the layer cake patterns observed after 6.7 Ma point to weaker currents, with lower oxygen levels but a more stable supply of organic matter to the seafloor, which agrees with the interpretation of Interval 2. The Tasman Sea presents a complex oceanographic setting and is in a key location, right in the middle of the return flow of the South Pacific Gyre. During the Late Miocene, the Pacific Ocean went through a major reorganization. Shankle et al. (2021) observed a decoupling between the zonal sea surface temperature gradient and biological productivity, and an increase in zonal pH gradient between 6 and 3 Ma in the tropical Pacific. They suggested that the enhanced ocean acidity in the east Pacific relative to the west Pacific could be related to the upwelling of older waters in the east associated with a large-scale reorganization of Pacific circulation. Models show that during this time interval, there was deep water formation in the North Pacific and an active PMOC, both of which are not present in the Pacific Ocean today (Burls et al., 2017). Moreover, the intensification of the Hadley and Walker circulation, due to the increased equator to pole temperature gradient, and the northward migration of the Westerlies and the ITCZ during this interval could have affected precipitation and river runoff, causing upwelling and ocean fertilization (Groeneveld et al., 2017; Herbert et al., 2016). Additionally, the global ocean cooling and the formation of sea ice around Antarctica would also have impacted the atmospheric circulation in the Southern Hemisphere, and this process must also have influenced and strengthened the Westerlies (Fan et al., 2014; Groeneveld et al., 2017).

These large-scale oceanographic changes, associated with the shift in the Westerlies must have influenced the EAC return flow into the southwest Pacific. Today, Site U1506 is located north of the eastern extension of the EAC, outside its area of influence. Groeneveld et al. (2017) suggested that during the Late Miocene (ca. 12–8 Ma) the Westerlies migrated northward reaching 30°S to 40°S, leading to wet conditions in Australia. We suggest that the northward migration of the Westerlies, and the consequent migration of the Hadley cell, led to the strengthening of the EAC and shallow-intermediate currents in the Tasman Sea during the Late Miocene, placing Site U1506 close to, or under, their influence. This process could explain the hydrographic conditions and strong bottom currents inferred in Interval 1 from the benthic foraminiferal assemblages and the seismic data. Such shorter-term frontal movements of western boundary currents related to shifting Westerlies have been documented for the Pliocene (e.g., Abell et al., 2021; Lam et al., 2021), and Pleistocene (e.g., Kawahata & Ohshima, 2002; Taylor et al., 2022).

The subsequent southward displacement and weakening of the Westerlies and Hadley cell could have led to a return to pre-Late Miocene oceanographic conditions, and thus weaker current activity at Site U1506, as documented in Interval 2. Additionally, the cooling and drying of the Asian landmass and the resulting intensification of the Asian winter monsoon during the Late Miocene could have increased the supply of nutrients, as reflected in conditions of increased productivity observed in Interval 2 (Holbourn et al., 2018). The strengthening and subsequent weakening of this subtropical western boundary current and of the intermediate waters during the Late Miocene explains the diverse expression of the Biogenic Bloom documented at Sites U1506 and 590.

4.4. The Biogenic Bloom: Tasman Sea Insights to a Global Perspective

The widespread nature of the Biogenic Bloom indicates that this event was not the result of unusual preservational artifact, and two models have been proposed to explain the increased primary productivity, although multiple factors may have played a role.

According to the first model, enhanced nutrient supply could have been related to increased runoff from land and nutrient availability in the oceans. Uplift of the Himalayas and intensification of the Asian monsoon-related weathering is one such mechanism suggested (Berger et al., 1993; Berger & Stax, 1994; Delaney & Filippelli, 1994; Farrell et al., 1995; Filipelli, 1997; Hermoyian & Owen, 2001).

Low estimates for uplift rates of the Himalayas after 10 Ma (Tada et al., 2016), however, partially weaken this hypothesis as decreased uplift rates would lead to decreased weathering and nutrient delivery. The role of the Indian and Asian monsoon, however, must not be overlooked as increased monsoonal activity may have affected ocean productivity, increasing nutrient input through rivers or strengthening seasonal winds and hence dust delivery and ocean upwelling (Filippelli, 1997; Holbourn et al., 2018; Kroon et al., 1991; Yang et al., 2019; Zhisheng et al., 2001).

The second model relies upon a major redistribution of nutrients within the oceans, related to changes in the ocean/atmosphere dynamics (Dickens & Owen, 1999). For example, Rind and Chandler (1991) linked the intensification of deep water formation in the north Atlantic between 9.0 and 3.0 Ma (Wright & Miller, 1996), and the high-latitude warming between 6.0 and 5.0 Ma (Koizumi, 1986) to an acceleration of the deep water conveyor. Moreover, high-latitude processes such as the silicic acid leakage could have moved silicic acid-rich Antarctic waters to the low latitudes and led to blooms of diatoms during cooling events and increased nutrients in surface waters (Brzezinski et al., 2002; Matsumoto et al., 2002; Matsumoto & Sarmiento, 2008). Early studies proposed a shift of nutrients from low to high-productivity regions caused by changes in ocean circulation. However, enhanced productivity conditions have also been recorded in oligotrophic regions of the Indian Ocean and the South Atlantic Ocean (Diester-Haass et al., 2005; Drury et al., 2021; Hermoyian & Owen, 2001). The global nature of the Biogenic Bloom challenges the hypothesis of redistribution of nutrients from the Atlantic Ocean into the Indian and Pacific oceans, even if ocean circulation changes likely played an important role in the Biogenic Bloom.

The widespread signal of this event suggests global forcing during the Late Miocene, but regional mechanisms account for differences in the expression and timing of the Biogenic Bloom. The common patterns and global nature of the Biogenic Bloom have been attributed to increased nutrient influx due to enhanced dust and/or increased weathering input, while the regional variability in the timing and amplitude of the event may arise from regional Late Miocene differences in sea surface temperatures, continental aridification and/or ocean circulation (Drury et al., 2021).

For instance, the reorganization of the climate-carbon cycle system with a reduction of Arctic continental carbon reservoirs during cooling intervals after 6 Ma (De Vleeschouwer et al., 2020), the expansion of C_4 grassland (Behrensmeyer et al., 2007; Cerling et al., 1997; Tauxe & Feakins, 2020; Uno et al., 2016), evidence for atmospheric pCO_2 decrease around ca. 8 to 7 Ma (Bolton & Stoll, 2013; Herbert et al., 2016; Tanner et al., 2020), the decrease in terrestrial and sea surface temperatures between 7 and 5 Ma (Herbert et al., 2016; Pound et al., 2011, 2012), and global changes in ocean circulation (Drury et al., 2017; Drury, Lee, et al., 2018; Reghellin et al., 2015, 2020) are examples of changes in the Late Miocene climate system that could have played a role in the Biogenic Bloom.

Recently, a global compilation of productivity records also indicated that a significant decrease in productivity ca. 4.6–4.4 Ma coincided with an orbital configuration that likely caused a decrease in East Asian Monsoon intensity

and nutrient input into the ocean, thereby bringing the main phase of Biogenic Bloom productivity to a close (Karatsolis et al., 2022). Due to low sediment recovery at Site U1506, it is difficult to resolve whether the main productivity phase of the event also ends ca. 4.6–4.4 Ma. However, LSRs and MAR_{Carb} dropped at Site U1506 at ca. 4.5 Ma and then just after ca. 3 Ma. The first drop in MAR_{Carb} around 4.5 Ma is in line with the global decrease in productivity documented by Karatsolis et al. (2022). But with MAR_{Carb} significantly declining again after 3 Ma, there is some indication that the Biogenic Bloom may continue into the Late Pliocene at U1506, which is also observed at Site 1264 (Figure 7a).

The onset of the Biogenic Bloom at ca. 7.8 Ma appears synchronous based on the increase in MAR_{Carb} at Site 1264 in the South Atlantic and in a stack of six equatorial Pacific sites (EEP), followed by a strong maximum ca. 7 Ma (Drury et al., 2021; Lyle et al., 2019). This pattern holds true at Site U1506, although the onset may occur slightly later (Figure 7a) or be biased due to lower recovery at this site. At Site U1506, MAR_{Carb} shows an increasing trend during Interval 1 and reaches a maximum at ca. 6.7 Ma, coinciding with the timing of the productivity regime change; during Interval 2, MAR_{Carb} remains high and shows a pattern similar to Site 1264 and to EEP.

At Site 1264, the onset of high MAR_{Carb} at ca. 7.8 Ma coincides with a shift from eccentricity–precession pacing to obliquity–precession pacing of $\%CaCO_3$ deposition (Drury et al., 2021). The rise in obliquity pacing was documented also in benthic $\delta^{18}O$ records as asymmetric cycles starting at ca. 7.7 Ma, strongly imprinted until ca. 6.7 Ma and likely linked to the increased influence of high-latitude climate processes and ice sheet dynamics on climate variability during the Late Miocene (De Vleeschouwer et al., 2020; Drury et al., 2017; Drury, Westerhold, et al., 2018). It is possible that this inferred increase in high-latitude climate processes between ca. 7.7 and 6.7 Ma caused increased nutrient input into the ocean through increased glacial weathering. This could be the underlying driver of the onset and broad peak in MAR_{Carb} ca. 7 Ma, which seems to be mirrored between our new Tasman Sea data (Site U1506), the South Atlantic (Site 1264) and the EEP (Figure 7a). The obliquity-driven cycles in benthic $\delta^{18}O$ become less pronounced after ca. 6.7 Ma (Drury et al., 2017; Drury, Westerhold, et al., 2018), which may have resulted in reduced glacial weathering and associated nutrient input, and the first stepped decrease in the Biogenic Bloom.

While the comparison of MAR_{Carb} allows us to speculate about the global mechanisms behind the event, the high-resolution study of the benthic foraminiferal assemblages at Site U1506 allows us to distinguish the regional/local imprint and to differentiate two phases (Interval 1 and Interval 2; Figure 7) during the Biogenic Bloom.

5. Conclusions

IODP Site U1506 in the Tasman Sea is a piece of a global puzzle important to understand some aspects of the Late Miocene-Early Pliocene Biogenic Bloom. At this site, we identified part of the Biogenic Bloom and we implemented the age model to calculate sedimentation rates and to date paleontological and geochemical changes across this event.

Benthic foraminifera assemblage point to two distinct productivity regimes within an overall scenario of high food supply to the seafloor. High nutrient availability at the seafloor is inferred from 7.4 to 6.7 Ma (Interval 1) based on high benthic foraminiferal accumulation rates (BFAR), high abundance of phytodetritus exploiting taxa, and opportunistic species. These results suggest high seasonal food supply, well-oxygenated bottom waters, and intense bottom currents. Between 6.7 and 4.5 Ma (Interval 2), the assemblages are dominated by dysoxic-suboxic taxa and infaunal morphogroups, pointing to high productivity triggered by continuous and high food supply to the seafloor and lower oxygen conditions. We speculate that the high productivity recorded during the event was possibly triggered by the increasing role played by high-latitude climate processes and ice sheet dynamics.

Our results also reveal that the diverse expression of the Biogenic Bloom from Interval 1 to Interval 2 seems to be related to the changes in the Pacific Ocean circulation during the Late Miocene. The productivity conditions and strong current activity documented in Interval 1 could be linked to a strengthening of the EAC and shallow-intermediate waters, driven by the northward migration of the Westerlies, and the consequent migration of the Hadley cell, which led to greater influence at Site U1506. In contrast, the subsequent southward movement of the Westerlies during Interval 2 resulted in a weakening of these currents and a reduced influence on the site, and accounts for the weaker current activity documented after 6.7 Ma. These results show the importance of high-resolution studies to distinguish the local, regional, and global imprint of the Biogenic Bloom.

Data Availability Statement

Data generated in this study are available in the Supporting Information S1 and archived in PANGAEA database (Gastaldello et al., 2023).

Acknowledgments
This work was funded by University of Padova DOR grant, CARIPARO Ph.D. scholarship, Fondazione Ing. Aldo Gini scholarship, and Grant PID2019-105537RB-I00 funded by MCIN/AEI/10.13039/501100011033 and by "ERDF A way of making Europe." This research used samples and data provided by the International Ocean Discovery Program (IODP). ED was funded by the Deutsche Forschungsgemeinschaft (DFG; Project number 273069579). Open Access Funding provided by Universita degli Studi di Padova within the CRUI-CARE Agreement.

References

Abell, J. T., Winckler, G., Anderson, R. F., & Herbert, T. D. (2021). Poleward and weakened westerlies during Pliocene warmth. *Nature*, *589*(7840), 70–75. https://doi.org/10.1038/s41586-020-03062-1

Alegret, L., Arreguín-Rodríguez, G. J., Trasviña-Moreno, C. A., & Thomas, E. (2021). Turnover and stability in the deep sea: Benthic foraminifera as tracers of Paleogene global change. *Global and Planetary Change*, *196*(2021), 103372. https://doi.org/10.1016/j.gloplacha.2020.103372

André, A., Weiner, A., Quillévéré, F., Aurahs, R., Morard, R., Douady, C. J., et al. (2013). The cryptic and the apparent reversed: Lack of genetic differentiation within the morphologically diverse plexus of the planktonic foraminifer globigerinoides sacculifer. *Paleobiology*, *39*(1), 21–39. https://doi.org/10.1666/0094-8373-39.1.21

Backman, J., Raffi, I., Rio, D., Fornaciari, E., & Pälike, H. (2012). Biozonation and biochronology of Miocene through Pleistocene calcareous nannofossils from low and middle latitudes. *Newsletters on Stratigraphy*, *45*(3), 221–244. https://doi.org/10.1127/0078-0421/2012/0022

Baird, M. E., Timko, P. G., Middleton, J. H., Mullaney, T. J., Cox, D. R., & Suthers, I. M. (2008). Biological properties across the Tasman Front off southeast Australia. *Deep Sea Research Part I: Oceanographic Research Papers*, *55*(11), 1438–1455. https://doi.org/10.1016/j.dsr.2008.06.011

Behrensmeyer, A. K., Quade, J., Cerling, T. E., Kappelman, J., Khan, I. A., Copeland, P., et al. (2007). The structure and rate of late Miocene expansion of C_4 plants: Evidence from lateral variation in stable isotopes in paleosols of the Siwalik Group, northern Pakistan. *Geological Society of America Bulletin*, *119*(11–12), 1486–1505. https://doi.org/10.1130/b26064.1

Berger, W. H., Leckie, R. M., Janecek, T. R., Stax, R., & Takayama, T. (1993). Neogene carbonate sedimentation on Ontong-Java-Plateau highlights and open questions. *Proceedings of Ocean Drilling Program Science Results*, *130*, 711–744. https://doi.org/10.2973/odp.proc.sr.130.051.1993

Berger, W. H., & Stax, R. (1994). Neogene carbonate stratigraphy of Ontong Java Plateau (western equatorial Pacific): Three unexpected findings. *Terra Nova*, *6*(5), 520–534. https://doi.org/10.1111/j.1365-3121.1994.tb00896.x

Berner, R. A. (1990). Atmospheric carbon dioxide levels over Phanerozoic time. *Science*, *249*(4975), 1382–1386. https://doi.org/10.1126/science.249.4975.1382

Bernhard, J. M. (1986). Characteristic assemblages and morphologies of benthic foraminifera from anoxic, organic-rich deposits; Jurassic through Holocene. *Journal of Foraminiferal Research*, *16*(3), 207–215. https://doi.org/10.2113/gsjfr.16.3.207

Bolton, C. T., & Stoll, H. M. (2013). Late Miocene threshold response of marine algae to carbon dioxide limitation. *Nature*, *500*(7464), 558–562. https://doi.org/10.1038/nature12448

Boscolo-Galazzo, F., Thomas, E., & Giusberti, L. (2015). Benthic foraminiferal response to the Middle Eocene climatic optimum (MECO) in the south-eastern Atlantic (ODP Site 1263). *Palaeogeography, Palaeoclimatology, Palaeoecology*, *417*, 432–444. https://doi.org/10.1016/j.palaeo.2014.10.004

Bostock, H. C., Opdyke, B. N., Gagan, M. K., & Fifield, L. K. (2004). Carbon isotope evidence for changes in Antarctic Intermediate Water circulation and ocean ventilation in the southwest Pacific during the last deglaciation. *Paleoceanography*, *19*(4). https://doi.org/10.1029/2004PA001047

Bown, P., & Young, J. (1998). Techniques. In P. R. Bown (Ed.), *Calcareous nannofossil biostratigraphy* (pp. 16–28). Chapman & Hall.

Brzezinski, M. A., Pride, C. J., Franck, V. M., Sigman, D. M., Sarmiento, J. L., Matsumoto, K., et al. (2002). A switch from Si $(OH)_4$ to NO_3^- depletion in the glacial Southern Ocean. *Geophysical Research Letters*, *29*(12), 5–1. https://doi.org/10.1029/2001GL014349

Burls, N. J., Fedorov, A. V., Sigman, D. M., Jaccard, S. L., Tiedemann, R., & Haug, G. H. (2017). Active Pacific meridional overturning circulation (PMOC) during the warm Pliocene. *Science Advances*, *3*(9), e1700156. https://doi.org/10.1126/sciadv.1700156

Cerling, T. E., Harris, J. M., MacFadden, B. J., Leakey, M. G., Quade, J., Eisenmann, V., & Ehleringer, J. R. (1997). Global vegetation change through the miocene/pliocene boundary. *Nature*, *389*(6647), 153–158. https://doi.org/10.1038/38229

Corliss, B. H., Brown, C. W., Sun, X., & Showers, W. J. (2009). Deep-sea benthic diversity linked to seasonality of pelagic productivity. *Deep Sea Research Part I: Oceanographic Research Papers*, *56*(5), 835–841. https://doi.org/10.1016/j.dsr.2008.12.009

De, S., & Gupta, A. K. (2010). Deep-sea faunal provinces and their inferred environments in the Indian Ocean based on distribution of recent benthic foraminifera. *Palaeogeography, Palaeoclimatology, Palaeoecology*, *291*(3–4), 429–442. https://doi.org/10.1016/j.palaeo.2010.03.012

De Almeida, F. K., De Mello, R. M., Costa, K. B., & Toledo, F. A. (2015). The response of deep-water benthic foraminiferal assemblages to changes in paleoproductivity during the Pleistocene (last 769.2 kyr), western South Atlantic Ocean. *Palaeogeography, Palaeoclimatology, Palaeoecology*, *440*, 201–212. https://doi.org/10.1016/j.palaeo.2015.09.005

Delaney, M. L., & Filippelli, G. M. (1994). An apparent contradiction in the role of phosphorus in Cenozoic chemical mass balances for the world ocean. *Paleoceanography*, *9*(4), 513–527. https://doi.org/10.1029/94PA00795

Dias, B. B., Barbosa, C. F., Faria, G. R., Seoane, J. C. S., & Albuquerque, A. L. S. (2018). The effects of multidecadal-scale phytodetritus disturbances on the benthic foraminiferal community of a Western Boundary Upwelling System, Brazil. *Marine Micropaleontology*, *139*, 102–112. https://doi.org/10.1016/j.marmicro.2017.12.003

Dickens, G. R., & Owen, R. M. (1994). Late Miocene-early Pliocene manganese redirection in the central Indian Ocean: Expansion of the intermediate water oxygen minimum zone. *Paleoceanography*, *9*(1), 169–181. https://doi.org/10.1029/93PA02699

Dickens, G. R., & Owen, R. M. (1999). The latest miocene-early pliocene biogenic bloom: A revised Indian Ocean perspective. *Marine Geology*, *161*(1), 75–91. https://doi.org/10.1016/S0025-3227(99)00057-2

Diester-Haass, L. (1995). Middle eocene to early oligocene paleoceanography of the Antarctic Ocean (Maud Rise, ODP Leg 113, Site 689): Change from a low to a high productivity ocean. *Palaeogeography, Palaeoclimatology, Palaeoecology*, *113*(2–4), 311–334. https://doi.org/10.1016/0031-0182(95)00067-v

Diester-Haass, L., Billups, K., & Emeis, K. C. (2005). In search of the late miocene–early pliocene "biogenic bloom" in the Atlantic Ocean (Ocean Drilling Program Sites 982, 925, and 1088). *Paleoceanography*, *20*(4), 20. https://doi.org/10.1029/2005PA001139

Diester-Haass, L., Billups, K., & Emeis, K. C. (2006). Late miocene carbon isotope records and marine biological productivity: Was there a (dusty) link? *Paleoceanography*, *21*(4). https://doi.org/10.1029/2006PA001267

Diester-Haass, L., Meyers, P. A., & Bickert, T. (2004). Carbonate crash and biogenic bloom in the late miocene: Evidence from ODP Sites 1085, 1086, and 1087 in the cape basin, southeast Atlantic Ocean. *Paleoceanography*, *19*(1). https://doi.org/10.1029/2003PA000933

Drury, A. J., John, C. M., & Shevenell, A. E. (2016). Evaluating climatic response to external radiative forcing during the late miocene to early pliocene: New perspectives from eastern equatorial Pacific (IODP U1338) and North Atlantic (ODP 982) locations. *Paleoceanography*, *31*(1), 167–184. https://doi.org/10.1002/2015PA002881

Drury, A. J., Lee, G. P., Gray, W. R., Lyle, M., Westerhold, T., Shevenell, A. E., & John, C. M. (2018). Deciphering the state of the late miocene to early pliocene equatorial Pacific. *Paleoceanography and Paleoclimatology*, *33*(3), 246–263. https://doi.org/10.1002/2017PA003245

Drury, A. J., Liebrand, D., Westerhold, T., Beddow, H. M., Hodell, D. A., Rohlfs, N., et al. (2021). Climate, cryosphere, and carbon cycle controls on Southeast Atlantic orbital-scale carbonate deposition since the Oligocene (30–0 Ma). *Climate of the Past*, *17*(5), 2091–2117. https://doi.org/10.5194/cp-17-2091-2021

Drury, A. J., Westerhold, T., Frederichs, T., Tian, J., Wilkens, R., Channell, J. E. T., et al. (2017). Late miocene climate and time scale reconciliation: Accurate orbital calibration from a deep-sea perspective. *Earth and Planetary Science Letters*, *475*, 254–266. https://doi.org/10.1016/j.epsl.2017.07.038

Drury, A. J., Westerhold, T., Hodell, D., & Röhl, U. (2018b). Reinforcing the North Atlantic backbone: Revision and extension of the composite splice at ODP site 982. *Climate of the Past*, *14*(3), 321–338. https://doi.org/10.5194/cp-14-321-2018

Eichler, P. P. B., Rodrigues, A. R., Gomes, M. P., & Vital, H. (2019). Benthic foraminifera as indicators of river discharge in the Western South Atlantic continental shelf. *Marine Geology*, *415*, 105973. https://doi.org/10.1016/j.margeo.2019.105973

Elmstrom, K. M., & Kennett, J. P. (1986). Late Neogene paleoceanographic evolution of site 590-southwest Pacific. *Initial Reports of the Deep Sea Drilling Project*, *90*, 1361–1381.

Erbacher, J., Hemleben, C., Huber, B. T., & Markey, M. (1999). Correlating environmental changes during early Albian oceanic anoxic event 1B using benthic foraminiferal paleoecology. *Marine Micropaleontology*, *38*(1), 7–28. https://doi.org/10.1016/S0377-8398(99)00036-5

Fan, T., Deser, C., & Schneider, D. P. (2014). Recent Antarctic sea ice trends in the context of Southern Ocean surface climate variations since 1950. *Geophysical Research Letters*, *41*(7), 2419–2426. https://doi.org/10.1002/2014gl059239

Farrell, J. W., Raffi, I., Janecek, T. R., Murray, D. W., Levitan, M., Dadey, K. A., et al. (1995). 35. Late Neogene sedimentation patterns in the eastern equatorial Pacific Ocean. In *Proceedings of the Ocean Drilling Program, Scientific Results* (Vol. 138). Ocean Drilling Program College Station.

Filippelli, G. M. (1997). Intensification of the Asian monsoon and a chemical weathering event in the late miocene–early pliocene: Implications for late Neogene climate change. *Geology*, *25*(1), 27–30. https://doi.org/10.1130/0091-7613(1997)025<0027:iotama>2.3.co;2

Fisher, R. A., Corbet, A. S., & Williams, C. B. (1943). The relation between the number of species and the number of individuals in a random sample of an animal population. *Journal of Animal Ecology*, *12*(1), 42. https://doi.org/10.2307/1411

Fontanier, C., Jorissen, F. J., Licari, L., Alexandre, A., Anschutz, P., & Carbonel, P. (2002). Live benthic foraminiferal faunas from the Bay of Biscay: Faunal density, composition, and microhabitats. *Deep Sea Research Part I: Oceanographic Research Papers*, *49*(4), 751–785. https://doi.org/10.1016/S0967-0637(01)00078-4

Gastaldello, M. E., Agnini, C., Westerhold, T., Drury, A. J., Sutherland, R., Drake, M. K., et al. (2023). Age model, geochemistry, XRF core scanning elemental data and benthic foraminifera from IODP Site 371-U1506 [Dataset]. PANGAEA. https://doi.org/10.1594/PANGAEA.953692

Gooday, A. J. (1988). A response by benthic foraminifera to the deposition of phytodetritus in the deep sea. *Nature*, *332*(6159), 70–73. https://doi.org/10.1038/332070a0

Gooday, A. J. (1993). Deep-sea benthic foraminiferal species which exploit phytodetritus: Characteristic features and controls on distribution. *Marine Micropaleontology*, *22*(3), 187–205. https://doi.org/10.1016/0377-8398(93)90043-W

Gooday, A. J. (2002). Biological responses to seasonally varying fluxes of organic matter to the ocean floor: A review. *Journal of Oceanography*, *58*(2), 305–332. https://doi.org/10.1023/A:1015865826379

Grant, K. M., & Dickens, G. R. (2002). Coupled productivity and carbon isotope records in the southwest Pacific Ocean during the late miocene–early pliocene biogenic bloom. *Palaeogeography, Palaeoclimatology, Palaeoecology*, *187*(1–2), 61–82. https://doi.org/10.1016/S0031-0182(02)00508-4

Groeneveld, J., Henderiks, J., Renema, W., McHugh, C. M., De Vleeschouwer, D., Christensen, B. A., & Expedition 356 Scientists. (2017). Australian shelf sediments reveal shifts in miocene southern hemisphere westerlies. *Science Advances*, *3*(5), e1602567. https://doi.org/10.1126/sciadv.1602567

Gupta, A. K., & Thomas, E. (1999). Latest miocene-pleistocene productivity and deep-sea ventilation in the northwestern Indian Ocean (Deep Sea Drilling Project Site 219). *Paleoceanography*, *14*(1), 62–73. https://doi.org/10.1029/1998pa900006

Hammer, Ø., Harper, D. A. T., & Ryan, P. D. (2001). Past: Paleontological statistics software package for education and data analysis. *Paleontologia Electronica*, *4*(1), 9. https://palaeo-electronica.org/2001_1/past/past.pdf

Hassler, C. S., Djajadikarta, J. R., Doblin, M. A., Everett, J. D., & Thompson, P. A. (2011). Characterisation of water masses and phytoplankton nutrient limitation in the East Australian Current separation zone during spring 2008. *Deep Sea Research Part II: Topical Studies in Oceanography*, *58*(5), 664–677. https://doi.org/10.1016/j.dsr2.2010.06.008

Hayward, B. W., Grenfell, H. R., Sabaa, A. T., Neil, H. L., & Buzas, M. A. (2010). Recent New Zealand deep-water benthic foraminifera: Taxonomy, ecologic distribution, biogeography, and use in paleoenvironmental assessment. *Geological & Nuclear Sciences Monograph* (Vol. 26, p. 363). Lower Hutt New Zealand.

Hayward, B. W., Sabaa, A. T., Grenfell, H. R., Neil, H., & Bostock, H. (2013). Ecological distribution of recent deep-water foraminifera around New Zealand. *Journal of Foraminiferal Research*, *43*(4), 415–442. https://doi.org/10.2113/gsjfr.43.4.415

Haywood, A. M., Dowsett, H. J., Valdes, P. J., Lunt, D. J., Francis, J. E., & Sellwood, B. W. (2009). Introduction. Pliocene climate, processes and problems. *Philosophical Transactions of the Royal Society A: Mathematical, Physical & Engineering Sciences*, *367*(1886), 3–17. https://doi.org/10.1098/rsta.2008.0205

Herbert, T. D., Lawrence, K. T., Tzanova, A., Peterson, L. C., Caballero-Gill, R., & Kelly, C. S. (2016). Late miocene global cooling and the rise of modern ecosystems. *Nature Geoscience*, *9*(11), 843–847. https://doi.org/10.1038/ngeo2813

Hermelin, J. O. R. (1989). In *Pliocene benthic foraminifera from the Ontong-Java plateau (western equatorial Pacific Ocean): Faunal response to changing paleoenvironments* (Vol. 26, pp. 1–143). Cushman Foundation for Foraminiferal Research Special Publication.

Hermoyian, C. S., & Owen, R. M. (2001). Late miocene-early pliocene biogenic bloom: Evidence from low-productivity regions of the Indian and Atlantic Oceans. *Paleoceanography*, *16*(1), 95–100. https://doi.org/10.1029/2000PA000501

Hodell, D. A., & Venz-Curtis, K. A. (2006). Late Neogene history of deepwater ventilation in the Southern Ocean. *Geochemistry, Geophysics, Geosystems*, *7*(9), Q09001. https://doi.org/10.1029/2005gc001211

Holbourn, A., Henderson, A. S., & MacLeod, N. (2013). *Atlas of benthic foraminifera*. John Wiley & Sons. https://doi.org/10.1002/9781118452493

Holbourn, A. E., Kuhnt, W., Clemens, S. C., Kochhann, K. G., Jöhnck, J., Lübbers, J., & Andersen, N. (2018). Late miocene climate cooling and intensification of southeast Asian winter monsoon. *Nature Communications*, *9*(1), 1–13. https://doi.org/10.1038/s41467-018-03950-1

Jorissen, F. J., Fontanier, C., & Thomas, E. (2007). *Paleoceanographical Proxies Based on Deep-Sea Benthic Foraminiferal Assemblage Characteristics* (Vol. 1). https://doi.org/10.1016/S1572-5480(07)01012-3

Kaiho, K. (1991). Global changes of Paleogene aerobic/anaerobic benthic foraminifera and deep-sea circulation. *Palaeogeography, Palaeoclimatology, Palaeoecology*, *83*(1–3), 65–85. https://doi.org/10.1016/0031-0182(91)90076-4

Kaiho, K. (1994). Benthic foraminiferal dissolved-oxygen index and dissolved-oxygen levels in the modern ocean. *Geology*, *22*(8), 719–722. https://doi.org/10.1130/0091-7613(1994)022<0719:bfdoia>2.3.co;2

Kaminski, M. A., & Gradstein, F. M. (2005). *Atlas of paleogene cosmopolitan deepwater agglutinated foraminifera*. The Grzybowski Foundation.

Kawahata, H., & Ohshima, H. (2002). Small latitudinal shift in the Kuroshio extension (Central Pacific) during glacial times: Evidence from pollen transport. *Quaternary Science Reviews*, *21*(14), 1705–1717. https://doi.org/10.1016/s0277-3791(01)00150-0

Kennett, J. P., & Von der Borch, C. C. (1986). Southwest Pacific cenozoic paleoceanography. *Initial Reports of the Deep Sea Drilling Project*, *90*, 1493–1517.

Koizumi, I. (1986). Pliocene and Pleistocene diatom datum levels related with paleoceanography in the northwest Pacific. *Marine Micropaleontology*, *10*(4), 309–325. https://doi.org/10.1016/0377-8398(86)90034-4

Kroon, D., Steens, T., & Troelstra, S. R. (1991). Onset of monsoonal related upwelling in the western Arabian Sea as revealed by planktonic foraminifers. In *Proceedings of the Ocean Drilling Program, Scientific Results* (Vol. 117, pp. 257–263). College Station, TX (Ocean Drilling Program).

Kump, L. R., & Arthur, M. A. (1999). Interpreting carbon-isotope excursions: Carbonates and organic matter. *Chemical Geology*, *161*(1–3), 181–198. https://doi.org/10.1016/s0009-2541(99)00086-8

Lam, A. R., MacLeod, K. G., Schilling, S. H., Leckie, R. M., Fraass, A. J., Patterson, M. O., & Venti, N. L. (2021). Pliocene to earliest Pleistocene (5–2.5 Ma) reconstruction of the Kuroshio current extension reveals a dynamic current. *Paleoceanography and Paleoclimatology*, *36*(9), e2021PA004318. https://doi.org/10.1029/2021PA004318

Liao, Y., & Lyle, M. (2014). Late miocene to pleistocene sedimentation and sediment transport on the Cocos Ridge, eastern tropical Pacific Ocean. *Marine Geology*, *355*, 1–14. https://doi.org/10.1016/j.margeo.2014.05.007

Lyle, M., Drury, A. J., Tian, J., Wilkens, R., & Westerhold, T. (2019). Late miocene to holocene high-resolution eastern equatorial Pacific carbonate records: Stratigraphy linked by dissolution and paleoproductivity. *Climate of the Past*, *15*(5), 1715–1739. https://doi.org/10.5194/cp-15-1715-2019

Marchesiello, P., & Middleton, J. H. (2000). Modeling the east Australian current in the Western Tasman Sea. *Journal of Physical Oceanography*, *30*(11), 2956–2971. https://doi.org/10.1175/1520-0485(2001)031<2956:mteaci>2.0.co;2

Martini, E. (1971). Standard Tertiary and Quaternary calcareous nannoplankton zonation. *Proceedings of the II Planktonic Conference, Roma*, 739–785.

Matsumoto, K., & Sarmiento, J. L. (2008). A corollary to the silicic acid leakage hypothesis. *Paleoceanography*, *23*(2). https://doi.org/10.1029/2007pa001515

Matsumoto, K., Sarmiento, J. L., & Brzezinski, M. A. (2002). Silicic acid leakage from the Southern Ocean: A possible explanation for glacial atmospheric pCO_2. *Global Biogeochemical Cycles*, *16*(3), 5–1. https://doi.org/10.1029/2001gb001442

Molnar, P., England, P., & Martinod, J. (1993). Mantle dynamics, uplift of the Tibetan Plateau, and the Indian monsoon. *Reviews of Geophysics*, *31*(4), 357–396. https://doi.org/10.1029/93rg02030

Mortimer, N., Campbell, H. J., Tulloch, A. J., King, P. R., Stagpoole, V. M., Wood, R. A., et al. (2017). Zealandia: Earth's hidden continent. *Geological Society of America Today*, *27*(3), 27–35. https://doi.org/10.1130/gsatg321a.1

Murray, J. W. (2006). *Ecology and applications of benthic foraminifera*. Cambridge University Press.

Naidu, P. D., & Malmgren, B. A. (1995). Do benthic foraminifer records represent a productivity index in oxygen minimum zone areas? An evaluation from the Oman Margin, Arabian Sea. *Marine Micropaleontology*, *26*(1–4), 49–55. https://doi.org/10.1016/0377-8398(95)00014-3

Nomura, R. (1995). *Paleogene to Neogene deep-sea paleoceanography in the eastern Indian Ocean: Benthic foraminifera from ODP Sites 747, 757 and 758* (pp. 251–290). Micropaleontology.

Okada, H., & Bukry, D. (1980). Supplementary modification and introduction of code numbers to the low-latitude coccolith biostratigraphic zonation (Bukry, 1973; 1975). *Marine Micropaleontology*, *5*, 321–325. https://doi.org/10.1016/0377-8398(80)90016-X

Oke, P. R., Pilo, G. S., Ridgway, K., Kiss, A., & Rykova, T. (2019). A search for the Tasman Front. *Journal of Marine Systems*, *199*, 103217. https://doi.org/10.1016/j.jmarsys.2019.103217

Peterson, L. C., Murray, D. W., Ehrmann, W. U., & Hempel, P. (1992). Cenozoic carbonate accumulation and compensation depth changes in the Indian Ocean. *Synthesis of Results from Scientific Drilling in the Indian Ocean*, *70*, 311–333.

Pound, M. J., Haywood, A. M., Salzmann, U., & Riding, J. B. (2012). Global vegetation dynamics and latitudinal temperature gradients during the mid to late miocene (15.97–5.33 Ma). *Earth-Science Reviews*, *112*(1–2), 1–22. https://doi.org/10.1016/j.earscirev.2012.02.005

Prell, W. L., & Kutzbach, J. E. (1992). Sensitivity of the Indian monsoon to forcing parameters and implications for its evolution. *Nature*, *360*(6405), 647–652. https://doi.org/10.1038/360647a0

Quade, J., & Cerling, T. E. (1995). Expansion of C4 grasses in the late miocene of northern Pakistan: Evidence from stable isotopes in paleosols. *Palaeogeography, Palaeoclimatology, Palaeoecology*, *115*(1–4), 91–116. https://doi.org/10.1016/0031-0182(94)00108-k

Rea, D. K., Basov, I. A., & Krissek, L. A., & the Leg 145 Scientific Party. (1995). Scientific results of drilling the North Pacific transect. *Proceedings of Ocean Drilling Program Science Results*, *145*, 577–596.

Reghellin, D., Coxall, H. K., Dickens, G. R., & Backman, J. (2015). Carbon and oxygen isotopes of bulk carbonate in sediment deposited beneath the eastern equatorial Pacific over the last 8 million years. *Paleoceanography*, *30*(10), 1261–1286. https://doi.org/10.1002/2015pa002825

Reghellin, D., Dickens, G. R., Coxall, H. K., & Backman, J. (2020). Understanding bulk sediment stable isotope records in the Eastern Equatorial Pacific, from seven million years ago to present day. *Paleoceanography and Paleoclimatology*, *35*(2). https://doi.org/10.1029/2019pa003586

Rind, D., & Chandler, M. (1991). Increased ocean heat transports and warmer climate. *Journal of Geophysical Research*, *96*(D4), 7437–7461. https://doi.org/10.1029/91jd00009

Schmiedl, G., Mackensen, A., & Müller, P. J. (1997). Recent benthic foraminifera from the eastern South Atlantic Ocean: Dependence on food supply and water masses. *Marine Micropaleontology*, *32*(3–4), 249–287. https://doi.org/10.1016/s0377-8398(97)00023-6

Schroder-Adams, C., Scott, D. B., & Medioli, F. S. (1987). Can smaller benthic foraminifera be ignored in paleoenvironmental analyses? *Journal of Foraminiferal Research*, *17*(2), 101–105. https://doi.org/10.2113/gsjfr.17.2.101

Shankle, M. G., Burls, N. J., Fedorov, A. V., Thomas, M. D., Liu, W., Penman, D. E., et al. (2021). Pliocene decoupling of equatorial Pacific temperature and pH gradients. *Nature*, *598*(7881), 457–461. https://doi.org/10.1038/s41586-021-03884-7

Singh, R. K., Gupta, A. K., & Das, M. (2012). Paleoceanographic significance of deep-sea benthic foraminiferal species diversity at southeastern Indian Ocean Hole 752A during the Neogene. *Palaeogeography, Palaeoclimatology, Palaeoecology*, *361*, 94–103. https://doi.org/10.1016/j.palaeo.2012.08.008

Smart, C. W., King, S. C., Gooday, A. J., Murray, J. W., & Thomas, E. (1994). A benthic foraminiferal proxy of pulsed organic matter paleofluxes. *Marine Micropaleontology*, *23*(2), 89–99. https://doi.org/10.1016/0377-8398(94)90002-7

Smart, C. W., Thomas, E., & Ramsay, A. T. (2007). Middle–late miocene benthic foraminifera in a western equatorial Indian Ocean depth transect: Paleoceanographic implications. *Palaeogeography, Palaeoclimatology, Palaeoecology*, *247*(3–4), 402–420. https://doi.org/10.1016/j.palaeo.2006.11.003

Stanton, B. R. (1981). An oceanographic survey of the Tasman Front. *New Zealand Journal of Marine & Freshwater Research*, *15*(3), 289–297. https://doi.org/10.1080/00288330.1981.9515924

Steinthorsdottir, M., Coxall, H. K., de Boer, A. M., Huber, M., Barbolini, N., Bradshaw, C. D., et al. (2021). The miocene: The future of the past. *Paleoceanography and Paleoclimatology*, *36*(4), e2020PA004037. https://doi.org/10.1029/2020PA004037

Suhr, S. B., Pond, D. W., Gooday, A. J., & Smith, C. R. (2003). Selective feeding by benthic foraminifera on phytodetritus on the western Antarctic Peninsula shelf: Evidence from fatty acid biomarker analysis. *Marine Ecology Progress Series*, *262*, 153–162. https://doi.org/10.3354/meps262153

Sutherland, R., Dickens, G. R., Blum, P., Agnini, C., Alegret, L., Bhattacharya, J., et al. (2018). International Ocean Discovery Program expedition 371 preliminary report: Tasman Frontier subduction initiation and paleogene climate. *Integrated Ocean Drilling Program: Preliminary Reports*(371).

Sutherland, R., Dos Santos, Z., Agnini, C., Alegret, L., Lam, A. R., Westerhold, T., et al. (2022). Neogene mass accumulation rate of carbonate sediment across northern Zealandia, Tasman Sea, southwest Pacific. *Paleoceanography and Paleoclimatology*, *37*(2), e2021PA004294. https://doi.org/10.1029/2021pa004294

Tada, R., Zheng, H., & Clift, P. (2016). Evolution and variability of the Asian monsoon and its potential linkage with uplift of the Himalaya and Tibetan Plateau. *Progress in Earth and Planetary Science*, *3*(1), 4. https://doi.org/10.1186/s40645-016-0080-y

Tanner, T., Hernández-Almeida, I., Drury, A. J., Guitián, J., & Stoll, H. (2020). Decreasing atmospheric CO_2 during the late Miocene cooling. *Paleoceanography and Paleoclimatology*, *35*(12), e2020PA003925. https://doi.org/10.1029/2020pa003925

Tauxe, L., & Feakins, S. J. (2020). A re-assessment of the chronostratigraphy of late miocene C3–C4 transitions. *Paleoceanography and Paleoclimatology*, *35*(7), e2020PA003857. https://doi.org/10.1029/2020PA003857

Taylor, S. P., Patterson, M. O., Lam, A. R., Jones, H., Woodard, S. C., Habicht, M. H., et al. (2022). Expanded North Pacific subtropical gyre and heterodyne expression during the mid-pleistocene. *Paleoceanography and Paleoclimatology*, *37*(5), e2021PA004395. https://doi.org/10.1029/2021PA004395

Toggweiler, J. R. (1999). Oceanography: An ultimate limiting nutrient. *Nature*, *400*(6744), 511–512. https://doi.org/10.1038/22892

Tomczak, M., & Godfrey, J. S. (1994). Regional oceanography: An introduction pergamon.

Uno, K. T., Polissar, P. J., Jackson, K. E., & de Menocal, P. B. (2016). Neogene biomarker record of vegetation change in eastern Africa. *Proceedings of the National Academy of Sciences*, *113*(23), 6355–6363. https://doi.org/10.1073/pnas.1521267113

Van Andel, T. H., Heath, G. R., & Moore, T. C. (1975). Cenozoic history and paleoceanography of the central equatorial Pacific Ocean: A regional synthesis of Deep Sea Drilling Project data.

Van Morkhoven, F. P. C. M., Berggren, W. A., Edwards, A. S., & Oertli, H. J. (1986). *Cenozoic cosmopolitan deep-water benthic Foraminifera*. Elf Aquitaine.

Vincent, E., Killingley, J. S., & Berger, W. H. (1980). The Magnetic epoch-6 carbon shift: A change in the ocean's 13C/12C ratio 6.2 million years ago. *Marine Micropaleontology*, *5*, 185–203. https://doi.org/10.1016/0377-8398(80)90010-9

Westerhold, T., Marwan, N., Drury, A. J., Liebrand, D., Agnini, C., Anagnostou, E., et al. (2020). An astronomically dated record of Earth's climate and its predictability over the last 66 million years. *Science*, *369*(6509), 1383–1387. https://doi.org/10.1126/science.aba6853

Wright, J. D., & Miller, K. G. (1996). Control of north Atlantic deep water circulation by the Greenland-Scotland ridge. *Paleoceanography*, *11*(2), 157–170. https://doi.org/10.1029/95pa03696

Yang, R., Yang, Y., Fang, X., Ruan, X., Galy, A., Ye, C., et al. (2019). Late miocene intensified tectonic uplift and climatic aridification on the northeastern Tibetan plateau: Evidence from clay mineralogical and geochemical records in the Xining basin. *Geochemistry, Geophysics, Geosystems*, *20*(2), 829–851. https://doi.org/10.1029/2018gc007917

Zachos, J., Pagani, M., Sloan, L., Thomas, E., & Billups, K. (2001). Trends, rhythms, and aberrations in global climate 65 Ma to present. *Science*, *292*(5517), 686–693. https://doi.org/10.1126/science.1059412

Zhisheng, A., Kutzbach, J. E., Prell, W. L., & Porter, S. C. (2001). Evolution of Asian monsoons and phased uplift of the Himalaya–Tibetan plateau since late miocene times. *Nature*, *411*(6833), 62–66. https://doi.org/10.1038/35075035

References From the Supporting Information

Agnini, C., Fornaciari, E., Raffi, I., Catanzariti, R., Pälike, H., Backman, J., & Rio, D. (2014). Biozonation and biochronology of Paleogene calcareous nannofossils from low and middle latitudes. *Newsletters on Stratigraphy*, *47*(2), 131–181. https://doi.org/10.1127/0078-0421/2014/0042

Backman, J., & Shackleton, N. J. (1983). Quantitative biochronology of Pliocene and early Pleistocene calcareous nannoplankton from the Atlantic, Indian and Pacific Oceans. *Marine Micropaleontology*, *8*(2), 141–170. https://doi.org/10.1016/0377-8398(83)90009-9

De Vleeschouwer, D., Drury, A. J., Vahlenkamp, M., Rochholz, F., Liebrand, D., & Pälike, H. (2020). High-latitude biomes and rock weathering mediate climate–carbon cycle feedbacks on eccentricity timescales. *Nature Communications*, *11*(1), 1–10. https://doi.org/10.1038/s41467-020-18733-w

Hayward, B. W., Grenfell, H. R., Sabaa, A. T., & Sikes, E. (2005). Deep-sea benthic foraminiferal record of the mid-Pleistocene transition in the SW Pacific. *Geological Society, London, Special Publications*, *247*(1), 85–115. https://doi.org/10.1144/GSL.SP.2005.247.01.05

Herguera, J. C., & Berger, W. (1991). Paleoproductivity from benthic foraminifera abundance: Glacial to postglacial change in the west-equatorial Pacific. *Geology*, *19*(12), 1173–1176. https://doi.org/10.1130/0091-7613(1991)019<1173:pfbfag>2.3.co;2

Hermelin, J. O. R. (1992). Variations in the benthic foraminiferal fauna of the Arabian sea: A response to changes in upwelling intensity? *Geological Society, London, Special Publications*, *64*(1), 151–166. https://doi.org/10.1144/gsl.sp.1992.064.01.10

Jorissen, F. J., de Stigter, H. C., & Widmark, J. G. (1995). A conceptual model explaining benthic foraminiferal microhabitats. *Marine Micropaleontology*, *26*(1–4), 3–15. https://doi.org/10.1016/0377-8398(95)00047-X

Karatsolis, B. T., Lougheed, B. C., De Vleeschouwer, D., & Henderiks, J. (2022). Abrupt conclusion of the late miocene-early pliocene biogenic bloom at 4.6-4.4 Ma. *Nature Communications*, *13*(1), 1–9. https://doi.org/10.1038/s41467-021-27784-6

Laskar, J., Robutel, P., Joutel, F., Gastineau, M., Correia, A. C. M., & Levrard, B. (2004). A long-term numerical solution for the insolation quantities of the Earth. *Astronomy & Astrophysics*, *428*(1), 261–285. https://doi.org/10.1051/0004-6361:20041335

Sutherland, R., Dickens, G. R., Blum, P., Agnini, C., Alegret, L., Asatryan, G., et al. (2019). Site U1506. In R. Sutherland, G. R. Dickens, & P. Blum (Eds.), *The expedition 371 scientists, Tasman Frontier subduction Initiation and Paleogene climate*, *Proceedings of the International Ocean Discovery Program* (Vol. 371). (International Ocean Discovery Program). https://doi.org/10.14379/iodp.proc.371.103.2019

Pound, M. J., Haywood, A. M., Salzmann, U., Riding, J. B., Lunt, D. J., & Hunter, S. J. (2011). A Tortonian (late Miocene, 11.61–7.25 Ma) global vegetation reconstruction. *Palaeogeography, Palaeoclimatology, Palaeoecology*, *300*(1–4), 29–45. https://doi.org/10.1016/j.palaeo.2010.11.029